

1-1-2012

# Quantification and Reconstruction in Photoacoustic Tomography

Zijian Guo

*Washington University in St. Louis*

Follow this and additional works at: <https://openscholarship.wustl.edu/etd>

---

## Recommended Citation

Guo, Zijian, "Quantification and Reconstruction in Photoacoustic Tomography" (2012). *All Theses and Dissertations (ETDs)*. 582.  
<https://openscholarship.wustl.edu/etd/582>

This Dissertation is brought to you for free and open access by Washington University Open Scholarship. It has been accepted for inclusion in All Theses and Dissertations (ETDs) by an authorized administrator of Washington University Open Scholarship. For more information, please contact [digital@wumail.wustl.edu](mailto:digital@wumail.wustl.edu).

WASHINGTON UNIVERSITY IN ST. LOUIS  
School of Engineering and Applied Science  
Department of Biomedical Engineering

Dissertation Examination Committee:

Lihong Wang, Chair  
Mark Anastasio  
Joseph Culver  
Robert Mach  
James Miller  
Lan Yang

Quantification and Reconstruction  
in Photoacoustic Tomography  
by  
Zijian Guo

A dissertation presented to the Graduate School of Arts and Sciences  
of Washington University in partial fulfillment of the  
requirements for the degree of

DOCTOR OF PHILOSOPHY

May 2012  
Saint Louis, Missouri

copyright by  
Zijian Guo  
2012

## ABSTRACT OF THE DISSERTATION

### Quantification and Reconstruction in Photoacoustic Tomography

by

Zijian Guo

Doctor of Philosophy in Biomedical Engineering

Washington University in St. Louis, 2012

Research Advisor: Professor Lihong Wang

Optical absorption is closely associated with many physiological important parameters, such as the concentration and oxygen saturation of hemoglobin. Conventionally, accurate quantification in PAT requires knowledge of the optical fluence attenuation, acoustic pressure attenuation, and detection bandwidth. We circumvent this requirement by quantifying the optical absorption coefficients from the acoustic spectra of PA signals acquired at multiple optical wavelengths. We demonstrate the method using the optical-resolution photoacoustic microscopy (OR-PAM) and the acoustical-resolution photoacoustic microscopy (AR-PAM) in the optical ballistic regime and in the optical diffusive regime, respectively.

The data acquisition speed in photoacoustic computed tomography (PACT) is limited by the laser repetition rate and the number of parallel ultrasound detecting channels. Reconstructing an image with fewer measurements can effectively accelerate the data acquisition and reduce the system cost. We adapted Compressed Sensing (CS) for the reconstruction in PACT. CS-based PACT was implemented as a non-linear conjugate gradient descent algorithm and tested with both phantom and *in vivo* experiments.

Speckles have been considered ubiquitous in all scattering-based coherent imaging technologies. As a coherent imaging modality based on optical absorption, photoacoustic

(PA) tomography (PAT) is generally devoid of speckles. PAT suppresses speckles by building up prominent boundary signals, via a mechanism similar to that of specular reflection. When imaging smooth boundary absorbing targets, the speckle visibility in PAT, which is defined as the ratio of the square root of the average power of speckles to that of boundaries, is inversely proportional to the square root of the absorber density. If the surfaces of the absorbing targets have uncorrelated height fluctuations, however, the boundary features may become fully developed speckles. The findings were validated by simulations and experiments. The first- and second-order statistics of PAT speckles were also studied experimentally. While the amplitude of the speckles follows a Gaussian distribution, the autocorrelation of the speckle patterns tracks that of the system point spread function.

# Acknowledgments

I would like to express my sincere gratitude to my thesis advisor, Professor Lihong Wang, for his invaluable advice and support. I thank him for inspiring me with challenging ideas, for helping me establish good research habits, for patiently correcting all my manuscripts, and for providing me an intellectually stimulating lab environment.

I thank my committee members, Prof. Mark Anastasio, Prof. Joseph Culver, Prof. Robert Mach, Prof. James Miller, and Prof. Lan Yang for their constructive suggestions and time given to serve on my thesis committee.

I am grateful for the excellent courses and seminars during my graduate studies at Rice University and Washington University in St. Louis. My sincere gratitude extends to all my teachers who taught me not only the knowledge to understand the world, but a curious mind to ask questions, and to explore the unknown domain.

I am deeply indebted to my collaborators, Christopher Favazza, Alejandro Garcia-Urbe, Li Li, Song Hu, Zhun Xu, Changhui Li, Liang Song, Todd Erpelding, Chulhong Kim, Yu Wang, Jun Xia, Liming Nie, Chatni Rameez, Haixin Ke, Xin Cai, and Chao Huang, for their support. The success of the research projects would not be possible without their great contributions.

No words can express my deep sense of gratitude to all my former and present colleagues for all their support, technical assistance, scientific discussions, and friendship over these years, in and outside the lab.

I am grateful for the financial support from McDonnell International Scholar Academy.

Thanks are due to James Ballard at Washington University for editing all my manuscripts.

With great love, I thank my family for their love and unfailing support throughout my career.

Zijian Guo

*Washington University in St. Louis*

*Dec 2011*

# Contents

<b>Abstract</b> .....	ii
<b>Acknowledgments</b> .....	iv
<b>List of Tables</b> .....	vii
<b>List of Figures</b> .....	viii
<b>List of Abbreviations</b> .....	ix
<b>1 Introduction</b> .....	1
1.1 Quantitative Photoacoustic Tomography (PAT) .....	1
1.2 Compressed Sensing in PAT .....	4
1.3 Speckles in PAT .....	5
<b>2 Quantitative PAT</b> .....	7
2.1 Quantification of Optical Absorption Coefficient from Acoustic Spectra .....	7
2.2 Quantification in the Optical Ballistic Regime.....	8
2.2.1 Quantification Model.....	9
2.2.2 Phantom Validations.....	10
2.2.3 <i>In Vivo</i> Studies.....	12
2.2.4 Discussion.....	14
2.3 Quantification in the Optical Diffusive Regime.....	15
2.3.1 Quantification Model.....	15
2.3.2 Phantom Validations.....	17
2.3.3 <i>In Vivo</i> Studies.....	19
2.3.4 Discussion.....	22
<b>3 Compressed Sensing in PAT</b> .....	23
3.1 Under-sampling in PAT .....	23
3.2 Application of the Compressed Sensing Theory in PAT .....	24
3.2.1 The Forward and Inverse Problems in PAT .....	24
3.2.2 Sparsity and Incoherence.....	26
3.2.3 Reconstruction Method.....	29
3.3 Results and Discussions .....	30
<b>4 Speckles in PAT</b> .....	35
4.1 On the Speckle-free Nature of PAT .....	35
4.1.1 Intuitive Explanation .....	36
4.1.2 Classic Speckle Theory Explanation.....	38
4.1.3 Mathematical Explanation.....	40

4.1.4	Simulation Studies .....	43
4.2	PAT Speckle Dependence on Boundary Roughness .....	47
4.3	Experimental Validations.....	52
4.4	Discussions and Conclusion.....	55
<b>5</b>	<b>Conclusions</b> .....	<b>57</b>
5.1	Summary of Work Done.....	57
5.2	Directions for Future Work.....	58
<b>Appendix A</b>	<b>Relative Sensitivity of DOT to Optical Absorption Coefficient ...</b>	<b>60</b>
<b>Appendix B</b>	<b>Validation of Equation (2.8) with Monte Carlo Simulations .....</b>	<b>54</b>
<b>Appendix C</b>	<b>Compressed Sensing Reconstruction Algorithm .....</b>	<b>66</b>
<b>Appendix D</b>	<b>Derivation of the Speckle Visibility Equation.....</b>	<b>68</b>
<b>Appendix E</b>	<b>Explanation of <math>\int_V h(\vec{r}, t -  \vec{r} /c) d\vec{r}^3 = 0</math> inside the structure.....</b>	<b>71</b>
<b>References</b>	.....	<b>73</b>
<b>Vita</b>	.....	<b>84</b>



# List of Tables

Table 2.1: Table 2.1 Quantified properties of blood vessels..... 14

# List of Figures

Figure 2.1 Schematic of the OR-PAM system and experimental setup.....	9
Figure 2.2 Quantification of the optical absorption coefficients of ink phantoms.....	11
Figure 2.3 Structural imaging and functional analysis with OR-PAM in a nude mouse ear <i>in vivo</i> .....	13
Figure 2.4 Schematic of the AR-PAM system and phantom experiment setups.....	16
Figure 2.5 Quantification of the optical absorption coefficients of oxygenated bovine blood phantom .....	18
Figure 2.6 Quantification of the sO <sub>2</sub> and [HbT]of blood vessels in the back of a nude mouse <i>in vivo</i> . .....	21
Figure 3.1 Illustration of the wavelet TPSF. ....	28
Figure 3.2 Tissue phantom imaging with a virtual point detector. ....	31
Figure 3.3 <i>In vivo</i> imaging of the mouse cortex with a circular ultrasonic array. ....	32
Figure 3.4 <i>In vivo</i> imaging of the upper dorsal region of a rat with a linear array. ....	33
Figure 4.1 Comparison of pulse-echo ultrasound imaging and reflection-mode PAT.....	37
Figure 4.2 Simulated depth profiles of a slab.....	44
Figure 4.3 Relationship between the speckle visibility in photoacoustic/ultrasound imaging and the absorber/scatterer density. ....	45
Figure 4.4 Simulated cross-sectional photoacoustic and ultrasonic images of round tumors. ....	46
Figure 4.5 Simulated PAT of absorbing objects with boundaries having various degrees of roughness at a spatial resolution of 180 μm.....	48
Figure 4.6 Effects of the RMS height ( $\delta$ ) and the correlation length ( $\xi$ ) on PA image boundaries .....	50
Figure 4.7 Phantom experiments.....	53
Figure 4.8 Experimental PA speckle statistics .....	54

# List of Abbreviations

2D:	Two dimensional
3D:	Three dimensional
ANSI:	American National Standards Institute
AR-PAM:	Acoustical resolution photoacoustic microscopy
B-scan:	Cross-sectional scan
CT:	Computed tomography
CW:	Continuous wave
CS:	Compressed sensing
DOT:	Diffuse optical tomography
FOV:	Field of view
FWHM:	Full width at half maxima
MRI:	Magnetic resonance imaging
NA:	Numerical aperture
NIR:	Near infrared
OCT:	Optical coherence tomography
OR-PAM:	Optical resolution photoacoustic microscopy
PA:	Photoacoustic
PAM:	Photoacoustic microscopy
PAT:	Photoacoustic tomography
PACT:	Photoacoustic computed tomography
PET:	Position emission tomography
RF:	Radio frequency
SNR:	Signal-to-noise ratio

# Chapter 1

## Introduction

### 1.1 Quantitative Photoacoustic Tomography (PAT)

Total, oxygenated, and deoxygenated hemoglobin concentrations ( $[\text{HbT}]$ ,  $[\text{HbO}_2]$ , and  $[\text{HbR}]$ ) are fundamental pathophysiological parameters in biomedicine. For example, abnormally low  $[\text{HbT}]$  may be caused by loss of blood, nutritional deficiency, chemotherapy, inflammation, kidney failure or bone marrow problems, while abnormally high  $[\text{HbT}]$  may be related to exposure to high altitude, smoking, dehydration and tumors. Blood oxygen saturation ( $s\text{O}_2$ ), which is defined as  $[\text{HbO}_2]$  divided by  $[\text{HbT}]$ , is vital in understanding brain hemodynamics in response to sensory stimulations, monitoring healing of burns [1] and wounds [2], and evaluating the effectiveness of chemotherapy and radiotherapy on tumors [3]. Several techniques have been developed to quantify hemoglobin concentration and  $s\text{O}_2$  *in vivo*, including diffuse optical tomography (DOT) and blood oxygen level dependent (BOLD) contrast magnetic resonance imaging (MRI). Positron emission tomography (PET) is used to monitor the oxygen metabolism. However, all of these modalities have disadvantages: for example, poor spatial resolution, relative quantification, and undesirable contrast agent injection [4, 5].

Photoacoustic (PA) tomography (PAT) can quantify hemoglobin concentrations *in vivo* based on endogenous contrast with both fine spatial resolution and high sensitivity [6]. In PAT, the sample is typically illuminated by a pulsed laser. Following the absorption of optical energy, an initial pressure is generated via thermo-elastic expansion. The initial pressure then propagates as ultrasonic waves, which are detected by ultrasonic sensors. The strength of the initial pressure  $P_0(\vec{r})$  in the unit of Pa at the location  $\vec{r}$  in the biological tissue is proportional to the local absorbed optical energy density  $A(\vec{r})$  in units of  $\text{J m}^{-3}$ . From multi-wavelength PA measurements, we can obtain the optical spectrum  $A(\vec{r}, \lambda)$  [i.e.,  $A(\vec{r})$  versus optical wavelength  $\lambda$ ], which can be used to quantify hemoglobin concentrations in the same way as DOT [7]. In the optical ballistic regime, the lateral resolution of PAT is determined by optical focusing [8], and thus it is comparable to that of other optical microscopy modalities. In the optical diffusive regime, however, the resolution of PAT is determined by ultrasonic waves [9], and PAT provides much better spatial resolution than DOT, in which the inverse algorithm is ill-posed. While DOT can only monitor  $\text{sO}_2$  which is volume-averaged over multiple blood vessels, PAT can pinpoint blood vessels and evaluate their individual  $\text{sO}_2$  levels [10]. Moreover, PAT inherently exploits optical absorption contrast, and thus it has a much higher sensitivity to optical absorption than other optical microscopy modalities [11] and DOT (see Appendix A).

Nevertheless, using PAT to quantify hemoglobin concentrations conventionally requires knowledge of the local optical fluence [12, 13]. In the quantification model, hemoglobin concentrations are derived [7] from the optical absorption coefficient  $\mu_a(\vec{r}, \lambda)$  in the unit of  $\text{m}^{-1}$  by solving the following equation for multiple values of  $\lambda$ :

$$\mu_a(\vec{r}, \lambda) = \varepsilon_{\text{HbR}}(\lambda)[\text{HbR}](\vec{r}) + \varepsilon_{\text{HbO}_2}(\lambda)[\text{HbO}_2](\vec{r}),$$

where  $\varepsilon_{\text{HbR}}(\lambda)$  and  $\varepsilon_{\text{HbO}_2}(\lambda)$  are the known molar extinction coefficients ( $\text{m}^{-1}\text{M}^{-1}$ ) of deoxyhemoglobin (HbR) and oxyhemoglobin (HbO<sub>2</sub>) at wavelength  $\lambda$ . Apart from spatial variation of the Grueneisen coefficient ( $\Gamma$ ) [6], PAT images, however, are spatial mappings of the absorbed optical energy density  $A(\vec{r}, \lambda) = \mu_a(\vec{r}, \lambda)F(\vec{r}, \lambda)$ , where

$F(\bar{r}, \lambda)$  represents the local optical fluence in units of  $\text{J m}^{-2}$ . To obtain the intrinsic quantity  $\mu_a(\bar{r}, \lambda)$  from  $A(\bar{r}, \lambda)$ , we need to quantify  $F(\bar{r}, \lambda)$ , which is usually unknown due to light transport in the scattering tissue.

$F(\bar{r}, \lambda)$  can be quantified *in vivo* either invasively [4] by inserting a calibration target or non-invasively [14-17] by using an auxiliary modality. In the invasive method, an exogenous optical absorber with known absorption spectrum  $\mu_a(\bar{r}', \lambda)$  is inserted at  $\bar{r}'$  near the target objects of interest. The PA amplitudes due to  $A(\bar{r}, \lambda)$  of the target objects of interest are normalized by the PA amplitude due to  $A(\bar{r}', \lambda)$  of the calibration target. By assuming  $F(\bar{r}', \lambda) \approx F(\bar{r}, \lambda)$ , we have

$$\mu_a(\bar{r}, \lambda) = \mu_a(\bar{r}', \lambda)A(\bar{r}, \lambda) / A(\bar{r}', \lambda).$$

This method physically compensates for the fluence attenuation; however, it is invasive. The non-invasive method involves solving both the optical diffusion equation and the PA wave equation iteratively. However, additional optical measurements are required, and the inverse algorithms are ill-posed.

The temporal profile of the PA signal has also been used to quantify optical absorption coefficients with reflection-mode PA imaging systems [18-21]. For example, if a pencil beam incident perpendicularly on the blood vessel surface, then the energy deposition in the vessel decays exponentially along the beam propagation direction. If at wavelength  $\lambda$  the reduced scattering coefficient  $\mu_s'(\lambda)$  is much smaller than the absorption coefficient  $\mu_a(\lambda)$  of blood, fitting the received PA signals with Beer's law yields  $\mu_a(\lambda)$ . Here, knowledge of the local optical fluence is not required, because  $\mu_a(\lambda)$  is quantified from the relative temporal decay profile. However, various acoustic effects may distort the received PA signals. Acoustic attenuation in biological tissue has a power law dependence on the frequency, and therefore the shapes of the acoustic pulses change as they propagate. Also, as ultrasonic detectors have limited bandwidths, the detected PA signal is the convolution of the received acoustic pulse and the mechanical-electrical impulse response of the detector. As such, the temporal profiles no longer

follow the exponential decay. Consequently, directly fitting the temporal profile for optical absorption coefficients can be inaccurate.

In Chapter 2, we discuss a method to quantify optical absorption coefficients from acoustic spectra measured at two optical wavelengths.

## 1.2 Compressed Sensing in PAT

By combining strong optical absorption contrast and high ultrasonic resolution in a single modality, PAT can achieve much better spatial resolution at depths beyond the optical ballistic regime ( $\sim 1$  mm in the skin) than the traditional optical modalities [6, 11]. When the excitation laser is replaced by microwave or RF sources, the technique is called thermoacoustic tomography (TAT) [22, 23]. Both PAT and TAT have been used successfully in a variety of applications, including high-quality *in vivo* vascular structural imaging, hemodynamic functional imaging [10, 24], and visualization of breast tumors [25, 26].

PAT has been implemented in various forms, and each form has its own advantages and applications [27]. In photoacoustic computed tomography (PACT, or simply PAT), an array of unfocused ultrasonic transducers is placed outside the object, and an inverse algorithm is used to reconstruct the image. Closed form reconstruction formulas have been reported in both the frequency and time domains for spherical, planar, and cylindrical detecting geometries [28-35]. However, a fundamental assumption of all these algorithms is that the spatial sampling of the detecting aperture is sufficient; otherwise, undersampling artifacts, such as streaking artifacts or grating lobes, appear.

Reliable image reconstruction with sparse sampling of the detecting aperture is desirable. In practical PAT systems, it is recommended [27, 36] to set the discrete spatial

sampling period to be two to five times smaller than the sensing aperture of the detector. For a scanning PAT system, it may require hundreds or even thousands of scanning steps to acquire an image, depending on the sizes of both the detector and the detecting aperture. Such scanning usually takes several minutes to complete. To reach real-time imaging, PAT is implemented with an array of ultrasonic transducers, where all or groups of the array elements can detect photoacoustic signals simultaneously. However, the data acquisition speed is still limited by the number of parallel data acquisition (DAQ) channels, and employing a large number of DAQ channels greatly increases the system cost. For example, for a fast 512-element ring array PAT system with a 64 channel data acquisition module [37], it takes 8 laser shots to collect data from all 512 elements. For direct 3-D reconstruction PAT applications [38, 39], the data from a 2-D ultrasonic array is usually an extremely sparse sampling of the detecting aperture. Moreover, channel crosstalk is also related to the space between neighboring elements (kerf), and an extensive spatial sampling may increase the crosstalk.

The recently developed compressed sensing (CS) theory enables us to eliminate the undersampling artifacts under certain conditions. The theory has been successfully applied in MRI, where MRI images were able to be reconstructed from significantly undersampled K-space measurements. In Chapter 3, we apply the CS theory in PAT [40].

### **1.3 Speckles in PAT**

Speckle has been considered ubiquitous in all coherent imaging modalities, such as laser imagery [41, 42], ultrasonography [43, 44], synthetic aperture radar, and optical [45] coherence tomography [46]. Fully developed speckle is formed by the interference among partial waves, either scattered from randomly distributed scatterers or reflected from a rough surface, whose phases are completely randomized over  $2\pi$ . The speckle



pattern generally has a high-contrast, fine-scale granular appearance, which does not correspond to the real structure of the sample. Although useful in certain applications, such as optical speckle imaging and ultrasound tissue characterization, speckle reduces both the effective spatial resolution and the detectability of small lesions, and thus deteriorates the image quality significantly. Many efforts have been made to mitigate this undesirable deterioration; however, speckle can be only partially reduced and only at the cost of system complexity, imaging time, or spatial resolution.

A long-standing conundrum is why photoacoustic tomography (PAT) possesses the unique ability to produce images devoid of speckle artifacts while all other coherent imaging technologies do not. We explain the reason and systematically study PAT speckles in Chapter 4.

# Chapter 2

## Quantitative PAT

### 2.1 Quantification of Optical Absorption Coefficient from Acoustic Spectra

We propose a method to quantify optical absorption coefficients from the acoustic spectra of multi-wavelength PA signals. The advantages include: 1) this method does not need fluence compensation, because the acoustic spectral profiles are independent of the absolute local optical fluence; 2) the same ultrasonic detector is employed for multiple optical wavelength measurements, and the acoustic properties of the tissue that lies between the target and the detector also remain unchanged. Therefore, the effects of the system bandwidth and the acoustic attenuation are eliminated.

Mathematically, the acoustic spectrum measured at wavelength  $\lambda$  of the received PA signal can be written, based on the linearity assumption, as [47]

$$S(\omega, \lambda) = F(\lambda)O(\omega, \lambda)a(\omega)H(\omega), \quad (2.1)$$

where  $\omega$  is the acoustic angular frequency and  $\lambda$  is the optical wavelength.  $F(\lambda)$  is the local optical fluence.  $O(\omega, \lambda)$  is the ‘real’ object spectrum measured with unit fluence, which is related to the target object’s shape, size, optical properties, and fluence incident directions.  $a(\omega)$  is the acoustic attenuation, which is related to the acoustic properties of the tissue that lies between the target objects and the detector.  $H(\omega)$  is the system

transfer function of the ultrasonic transducer, which is the Fourier transform of the PA signal from an ideal point absorber measured with this system. The last two terms remain unchanged when samples are measured with the same system under the same condition, and therefore are usually cancellable. Here the same condition means the acoustic properties of the tissue between the sample and the detectors are the same. An obvious example is where various optical wavelengths are used to excite one blood vessel. Therefore, simply dividing the PA acoustic spectrum measured at one optical wavelength by the spectrum measured at another wavelength, we can eliminate the system dependent effects and the acoustic attenuation effect:

$$\frac{S(\omega, \lambda_1)}{S(\omega, \lambda_2)} = \frac{F(\lambda_1)O(\omega, \lambda_1)a(\omega)H(\omega)}{F(\lambda_2)O(\omega, \lambda_2)a(\omega)H(\omega)} = \frac{F(\lambda_1)O(\omega, \lambda_1)}{F(\lambda_2)O(\omega, \lambda_2)}. \quad (2.2)$$

The absolute values of  $\mu_a(\lambda_1)$  and  $\mu_a(\lambda_2)$  as well as the ratio of  $F(\lambda_1)$  to  $F(\lambda_2)$  are derived by fitting the ratio of the spectra. As such, the absolute value of  $\mu_a$  can be quantified with this method even though  $F(\lambda)$  varies with the optical wavelength. By contrast, previous methods [4, 12, 14, 15, 48, 49] can quantify only the relative value of  $\mu_a$ .

With the knowledge of  $\mu_a(\lambda_1)$  and  $\mu_a(\lambda_2)$ , sO<sub>2</sub> levels are calculated [7] by solving the following equation for multiple values of  $\lambda$ :

$$\mu_a(\bar{r}, \lambda) = \varepsilon_{\text{HbR}}(\lambda)[\text{HbR}](\bar{r}) + \varepsilon_{\text{HbO}_2}(\lambda)[\text{HbO}_2](\bar{r}), \quad (2.3)$$

where  $\varepsilon_{\text{HbR}}(\lambda)$  and  $\varepsilon_{\text{HbO}_2}(\lambda)$  are the known molar extinction coefficients ( $\text{m}^{-1}\text{M}^{-1}$ ) of deoxyhemoglobin HbR and oxyhemoglobin HbO<sub>2</sub> at wavelength  $\lambda$ .

## 2.2 Quantification in the Optical Ballistic Regime

## 2.2.1 Quantification Model

As the first feasibility study, we validated this idea using one form of PA imaging, optical resolution photoacoustic microscopy (OR-PAM) [50], where the object spectrum  $O(\omega, \lambda)$  can be relatively easily modeled.

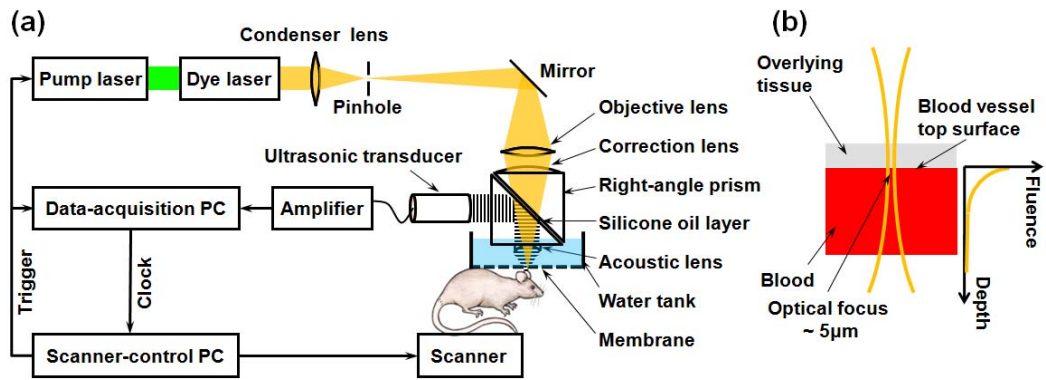


**Figure 2.1 Schematic of the OR-PAM system and experimental setup.** (a) A dye laser pumped by a Nd:YLF laser is used as the irradiation source. The laser beam from the dye laser is spatially filtered by a pinhole and then focused by an objective lens. Ultrasonic focusing is achieved through a plano-concave lens. The optical objective lens and 50 MHz ultrasonic transducer are confocally configured. Volumetric images are generated through a combination of time-resolved detection of the PA waves with a two-dimensional raster scanning in the transverse plane. (b) The optical focus is much smaller than the targeted blood vessel, whose top surface within the optical focal diameter can therefore be approximated as a plane. The optical fluence within the blood vessel decays exponentially with depth at a rate of the optical absorption coefficient.

In OR-PAM, PA A-scan signals are acquired through time-resolved ultrasonic detection, and three-dimensional images were formed by raster scanning the ultrasonic transducer along the transverse plane [Fig. 2.1(a)]. The axial resolution of the system depended on the ultrasonic transducer bandwidth (centered at 50 MHz with 80% bandwidth), while the lateral resolution relied on optical focusing, which can reach the

theoretical optical diffraction limit. For the system we used, the axial and lateral resolutions were quantified to be 15  $\mu\text{m}$  and 5  $\mu\text{m}$ , respectively. Therefore, the surface of blood vessels with  $>30 \mu\text{m}$  diameter can be roughly treated as a flat surface. In this case, the acoustic spectrum of the generated PA signal is only related to the optical penetration depth. If we use  $F_0$  to denote the incident fluence on the surface of the blood vessel, the fluence inside the blood vessel obeys Beer's law and can be written as  $F(z) = F_0 \exp(-\mu_a z)$  [Fig. 2.1(b)]. Here the reduced scattering coefficient is neglected, since  $\mu_s'$  is much smaller than  $\mu_a$  in blood in the optical spectral region typically used.

The PA signal generated by the object

$$O(t, \lambda) = \mu_a \exp[-\mu_a(\lambda)ct], \quad (2.4)$$

where  $c$  is the speed of sound in the biological tissue. Fourier transformation of Eq. (2.4) leads to

$$|O(\omega, \lambda)| = \frac{1}{\sqrt{(\omega / \mu_a)^2 + c^2}}. \quad (2.5)$$

If the PA signals of the blood vessel are measured at two optical wavelengths, the ratio of the spectra of the PA signals can be written as

$$\frac{S(\omega, \lambda_1)}{S(\omega, \lambda_2)} = \frac{F(\lambda_1)O(\omega, \lambda_1)H(\omega)a(\omega)}{F(\lambda_2)O(\omega, \lambda_2)H(\omega)a(\omega)} = \frac{F(\lambda_1)\sqrt{[\omega / \mu_a(\lambda_2)]^2 + c^2}}{F(\lambda_2)\sqrt{[\omega / \mu_a(\lambda_1)]^2 + c^2}}. \quad (2.6)$$

By fitting this ratio we can derive the absolute values of  $\mu_a(\lambda_1)$ ,  $\mu_a(\lambda_2)$ , and  $F(\lambda_1) / F(\lambda_2)$ .

## 2.2.2 Phantom Validations

In a phantom study, the original black ink was diluted with water in six ratios ranging from 1:1 to 1:6. The original and diluted ink samples were sequentially placed in a container, sealed with plastic membrane, and then the container was placed in a water

tank. PA A-line signals were acquired from these samples, and the acoustic spectra of the PA signals are shown in Fig. 2.2(a). Compared with the spectrum of the PA signal from the original ink sample, the spectra of the PA signals from the diluted ink samples are “shifted” to lower frequencies. Light penetrated deeper in lower concentration ink samples, and the corresponding PA signals decay more slowly in the time domain. Therefore, the spectra contain more low-frequency components.

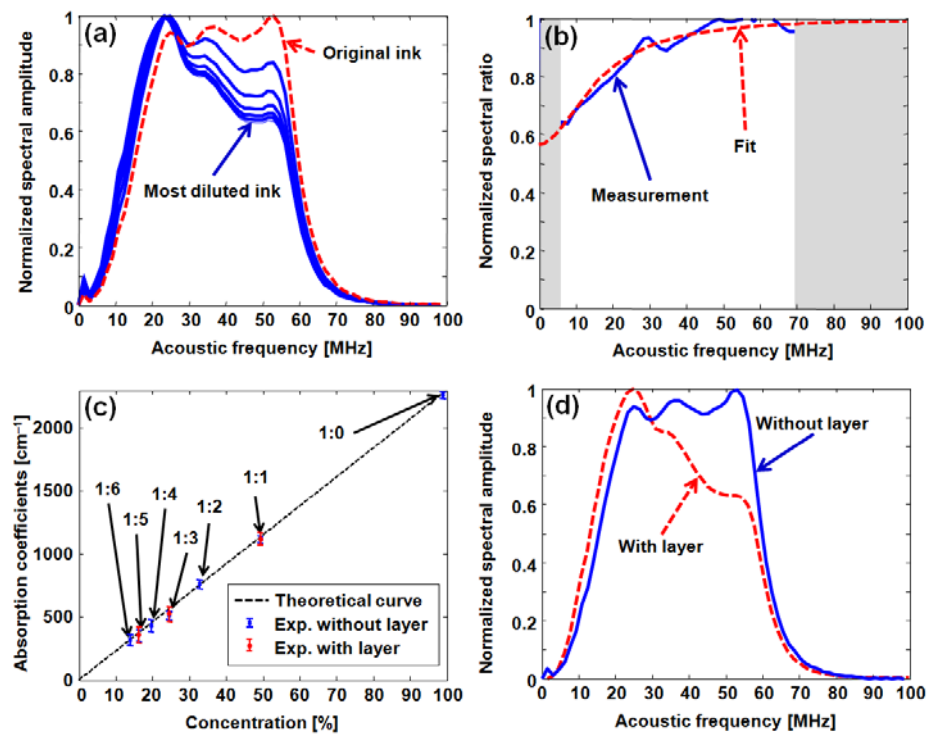


**Figure 2.2 Quantification of the optical absorption coefficients of ink phantoms.**

(a) Acoustic spectra of PA signals from original and diluted black ink samples. (b) Ratio of the acoustic spectrum amplitudes of PA signals from two samples and fitting with the theoretical formula. (c) Fitting result with 7 phantoms (without the covered layer) and 3 samples (with the covered layer). (d) The effect of acoustic attenuation was observed by covering one sample with  $\sim 1.5$  mm layer of Agar gel mixed with 0.1% Intralipid and 1% black ink.

By dividing the measured spectra of any two ink samples frequency-by-frequency [Fig. 2.2(b)], we can find the absorption coefficients of both samples by fitting the resultant ratio curve with Eq. (2.6). Because parts of the spectra (grey bands) are unreliable due to the limited bandwidth detection, they are not used for the fitting. By pairing the spectrum from the 1:1 diluted ink sample with the spectra from other six samples, we quantified the absorption coefficients of all seven samples. The quantified values and their theoretical predictions are plotted in Fig. 2.2(c). The error bars indicate the fitting standard deviations.

To demonstrate that the recovered absorption coefficients are independent of acoustic attenuation and optical fluence, we covered three of the ink samples with an identical layer of optical phantom ( $\sim 1.5$  mm 2% Agar, 0.1% intralipid, 1% black ink). The spectra of the PA signals from one ink sample with and without this layer are shown in Fig. 2.2(d). The spectral profiles differ because of the acoustic attenuation, while the spectral magnitudes differ owing to the optical fluence attenuation. Since the acoustic properties of the layer added between the samples and the detector are the same for the three ink samples, the acoustic attenuation can be cancelled by taking the ratio of the acoustic spectra of PA signals from any two covered ink samples. The quantified absorption coefficients of these samples agree with the expected values as shown in Fig. 2.2(c).

### 2.2.3 *In Vivo* Studies

In an *in vivo* experiment, we imaged a 1-mm-by-1-mm region in a nude mouse ear with two optical wavelengths (561 nm and 570 nm). Figure 3 (a) shows the PA maximum amplitude projection (MAP) image acquired with an optical wavelength of 570 nm, an oxygen insensitive absorption wavelength of hemoglobin. Each point in the MAP image records the maximum value of a Hilbert transformed PA A-scan. Two vessels marked with  $V_1$  and  $V_2$  in Fig. 2.3 (a) were selected for quantitative study. The A-scans acquired within these two vessels were properly aligned and then averaged. For each vessel, we

divide point by point the acoustic spectrum measured at 561 nm by the acoustic spectrum measured at 570 nm, and the absorption coefficients are acquired by fitting the ratio with Eq. (2.6) [Fig. 2.3 (b)]. The [HbT], [HbO<sub>2</sub>], and [HbR], together with the sO<sub>2</sub> values were calculated based on the quantified optical absorption coefficients at the two optical wavelengths (Table 2.1). According to the sO<sub>2</sub> values, V<sub>1</sub> and V<sub>2</sub> were identified to be an arteriole-venule pair. The incident fluence ratio at the two optical wavelengths  $F(\lambda_1)/F(\lambda_2)$  was also quantified for both vessels. In this special case, the two vessels are embedded at a similar depth, and the optical and the acoustic properties of the overlying tissue are comparable. Here, the quantified fluence ratios turned out to be the same for V<sub>1</sub> and V<sub>2</sub>. If we ignore the wavelength-dependent fluence variations by simply assuming  $F(\lambda_1)/F(\lambda_2)=1$ , the quantified sO<sub>2</sub> values become inaccurate by approximately 8% and 11% for the artery and the vein, respectively (Table 2.1).

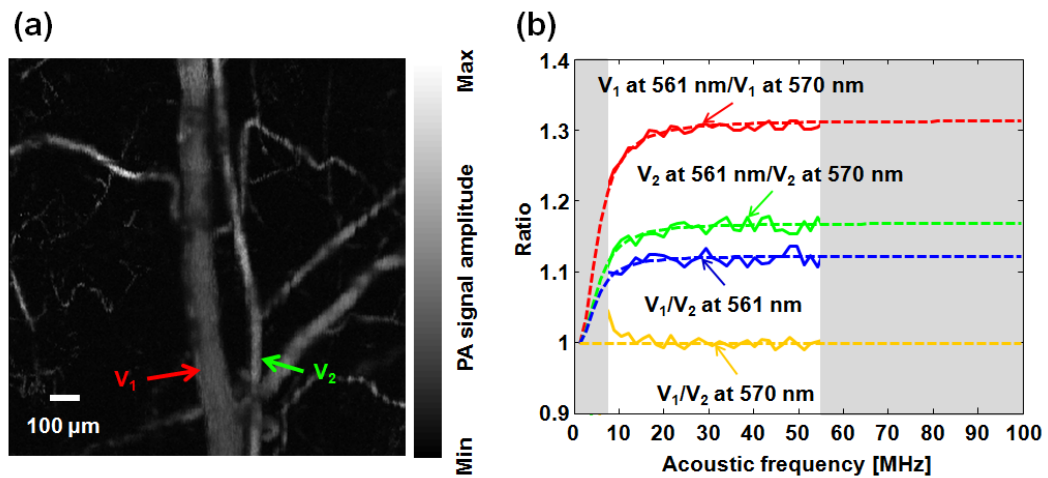


**Figure 2.3 Structural imaging and functional analysis with OR-PAM in a nude mouse.** (a) Structural image acquired at 570 nm. (b) Ratios of the acoustic spectrum amplitudes of PA signals measured with two optical wavelengths (570 nm and 561 nm) from arteries and veins.



**Table 2.1 Quantified properties of blood vessels**

	$\mu_a(\lambda_1)$ ( $\text{cm}^{-1}$ )	$\mu_a(\lambda_2)$ ( $\text{cm}^{-1}$ )	$F(\lambda_2)/F(\lambda_1)$	[HbT] (g/L)	[HbO <sub>2</sub> ] (g/L)	[HbR] (g/L)	sO <sub>2</sub>	sO <sub>2</sub> With $F(\lambda_2)/F(\lambda_1) = 1$
<b>V<sub>1</sub> (Artery)</b>	143±3	188±4	0.96±0.01	110.6±8.1	106.2±4.3	4.4±3.8	0.96±0.04	0.88
<b>V<sub>2</sub> (Vein)</b>	159±4	186±5	0.96±0.01	110.2±9.2	77.1±4.9	33.1±4.3	0.70±0.07	0.62

Moreover, because  $H(\omega)$  is dependent on only the imaging system and  $a(\omega)$  is also roughly the same for both vessels, the optical absorption coefficients of both vessels can be quantified with a single optical wavelength (561 nm) measurement. We divide the acoustic spectrum measured from V<sub>1</sub> by the acoustic spectrum measured from V<sub>2</sub> at 561 nm point by point and fit the ratio for the  $\mu_a$  values of both blood vessels [Fig. 2.3 (b)]. The fitted  $\mu_a$  values are  $143\pm 4 \text{ cm}^{-1}$  and  $159\pm 4 \text{ cm}^{-1}$  for V<sub>1</sub> and V<sub>2</sub>, which agree with the values in Table 2.1.

## 2.2.4 Discussions

To ensure the accuracy of this method, it is important to choose an ultrasonic transducer with an appropriate bandwidth. According to the sensitivity analysis (see Supplementary material), this method can achieve better sensitivity at higher acoustic frequencies. However, other factors need to be considered as well. First, the acoustic spectrum of the PA signal is related to the light penetration depth. Therefore, the central frequency of the transducer needs to match the penetration depth to achieve the best signal to noise ratio (SNR). Moreover, SNR is usually low at high acoustic frequencies due to acoustic attenuation.  $O(\omega, \lambda)$ ,  $H(\omega)$  and  $a(\omega)$  are all band-limited, and  $H(\omega)$  should be chosen to match  $O(\omega, \lambda)$  and  $a(\omega)$ . Second, the PA method is usually sensitive to boundaries of absorbing objects [51], and this method uses only the top boundaries of the blood vessels. Therefore, it requires that the top and bottom boundaries of the blood vessel to be resolvable. Accordingly, the blood vessel diameter must be greater than two times of the axial resolution, which is closely related to the

transducer bandwidth. This requirement usually can be relaxed, because of the limited light penetration depth in blood ( $\sim 30 \mu\text{m}$  in Q-band). The axial resolution of our OR-PAM is  $15 \mu\text{m}$ , and thus this method can work well when imaging blood vessels with diameters greater than  $30 \mu\text{m}$  with our system.

In summary, we demonstrated the feasibility of using the acoustic spectrum information to quantify optical absorption *in vivo* with OR-PAM. To the best of our knowledge, this is the first time acoustic spectrum information was used for PA quantitative study. This method is self-calibrating and thus is insensitive to absolute optical fluence. By taking advantage of the cancellation effect, the acoustic attenuation and system limited bandwidth can be corrected with multi-wavelength measurements. Moreover, this method can quantify the absolute value of  $\mu_a$ , which can be used to quantify hemoglobin concentrations in absolute units.

## 2.3 Quantification in the Optical Diffusive Regime

### 2.3.1 Quantification Model

We applied this idea to acoustic-resolution PA microscopy (AR-PAM) [10]. Figure 2.4(a) shows the AR-PAM system. A dye laser pumped by a Nd:YLF laser served as the irradiation source. At each location, a focused ultrasonic transducer was employed to record the PA wave, which was converted into a one-dimensional (1D) depth-resolved image (A-scan or A-line). A three-dimensional (3D) image was achieved by raster scanning in the x-y plane. The lateral resolution of the AR-PAM, determined by the focal diameter of the ultrasonic transducer, was  $\sim 45 \mu\text{m}$  for the 50 MHz transducer.

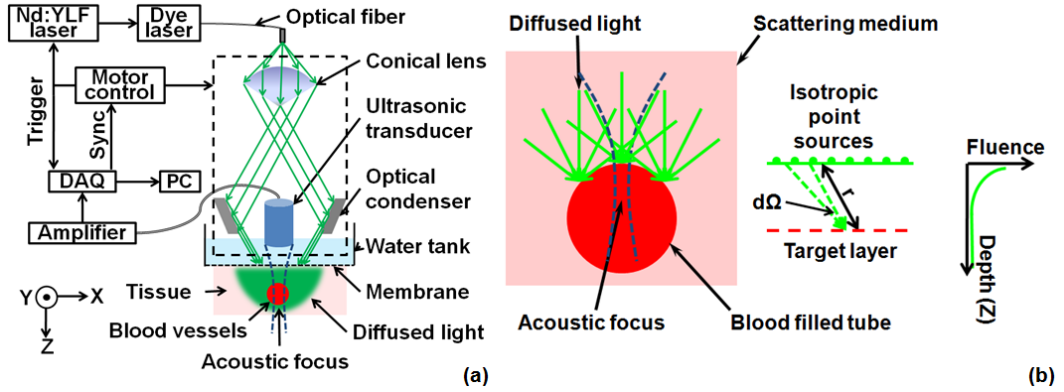


**Figure 2.4 Schematic of the AR-PAM system and phantom experiment setups.**

(a) The schematic of the AR-PAM system. A dye laser pumped by a Nd:YLF laser was the irradiation source. The laser beam from the dye laser was delivered through an optical fiber and passes through a conical lens to provide a ring-shaped area of illumination. A focused ultrasonic transducer was employed to detect PA waves. (b) Use AR-PAM to image a blood-filled tube inserted 1.5 mm deep in the optical scattering medium.

With AR-PAM, however, several assumptions can simplify the modeling of  $O(t, \lambda)$ . First, the surface of blood vessels with sufficiently large diameters (e.g., greater than 300  $\mu\text{m}$  for the 45  $\mu\text{m}$  lateral resolution) may be treated approximately as a flat surface locally. Second, when imaging blood vessels at depths greater than one transport mean free path ( $l_t' \sim 1$  mm in biological tissue), we can assume that the light is completely diffused and can be considered as isotropic point sources [Fig. 2.4(b)]. The fluence in the blood vessel can be expressed as

$$F(z, \lambda) = F(\lambda) \int_{\Omega} \exp[-\mu_a(\lambda)r] \frac{d\Omega}{2\pi}, \quad (2.7)$$

where  $z$  is the depth of the target layer in the blood vessel,  $r$  is the distance between the isotropic point source and one point in the layer at the depth of  $z$ , and  $F(\lambda)$  is the incident fluence on the blood vessel.  $d\Omega = \sin\theta d\theta d\varphi$  is the unit solid angle in the spherical coordinates, and the integration ranges of the polar angle  $\theta$  and the azimuthal

angle  $\varphi$  are  $[0, \pi/2]$  and  $[0, 2\pi]$ , respectively. Here,  $\mu_s'(\lambda)$  is much less than  $\mu_a(\lambda)$ , because the anisotropy factor ( $g$ ) is so close to 1 in blood in the optical spectral region we used (around 585 nm) [52]; therefore it is neglected. Equation (2.7) can be further simplified to

$$F(z, \lambda) = F(\lambda) \int_0^1 \exp[-\mu_a(\lambda)z/u] du, \quad (2.8)$$

where  $u$  is a dimensionless scaling factor defined by  $u = z/r$ . Equation (2.8) was validated by Monte Carlo simulations [53] (see Appendix B). The original PA signal from the target object induced by unit incident optical fluence is expressed as

$$O(t, \lambda) = \Gamma \mu_a(\lambda) F(z, \lambda) / F_i(\lambda) = \Gamma \mu_a(\lambda) \int_0^1 \exp[-\mu_a(\lambda)ct/u] du,$$

where  $z$  is converted to time  $t$  through the speed of sound  $c$ :  $t = z/c$ .

Similar to the case of OR-PAM [47], the effects of both the system-dependent response  $H(\omega)$  and the tissue related acoustic attenuation  $a(\omega)$  are canceled by dividing, at each acoustic frequency, the acoustic spectra measured at two optical wavelengths as

$$\frac{S(\omega, \lambda_1)}{S(\omega, \lambda_2)} = \frac{F(\lambda_1)O(\omega, \lambda_1)a(\omega)H(\omega)}{F(\lambda_2)O(\omega, \lambda_2)a(\omega)H(\omega)} = \frac{F(\lambda_1)O(\omega, \lambda_1)}{F(\lambda_2)O(\omega, \lambda_2)}. \quad (2.9)$$

Fitting the above spectral ratio yields the absolute values of  $\mu_a(\lambda_1)$  and  $\mu_a(\lambda_2)$  as well as the ratio of  $F(\lambda_1)$  to  $F(\lambda_2)$ .

### 2.3.2 Phantom Validations

In a phantom study, we used AR-PAM to image a fully oxygenated bovine blood phantom with four wavelengths (560, 565, 570, and 575 nm), where the absorption coefficients monochromatically increase  $[\mu_a(560) < \mu_a(565) < \mu_a(570) < \mu_a(575)]$ . The blood phantom was in a 1 mm diameter tube, which was located 1.5 mm deep in the optical scattering medium (10% gelatin, 1% intralipid, 5% CuCl<sub>2</sub>) and parallel to its surface [Fig. 2.4(b)].

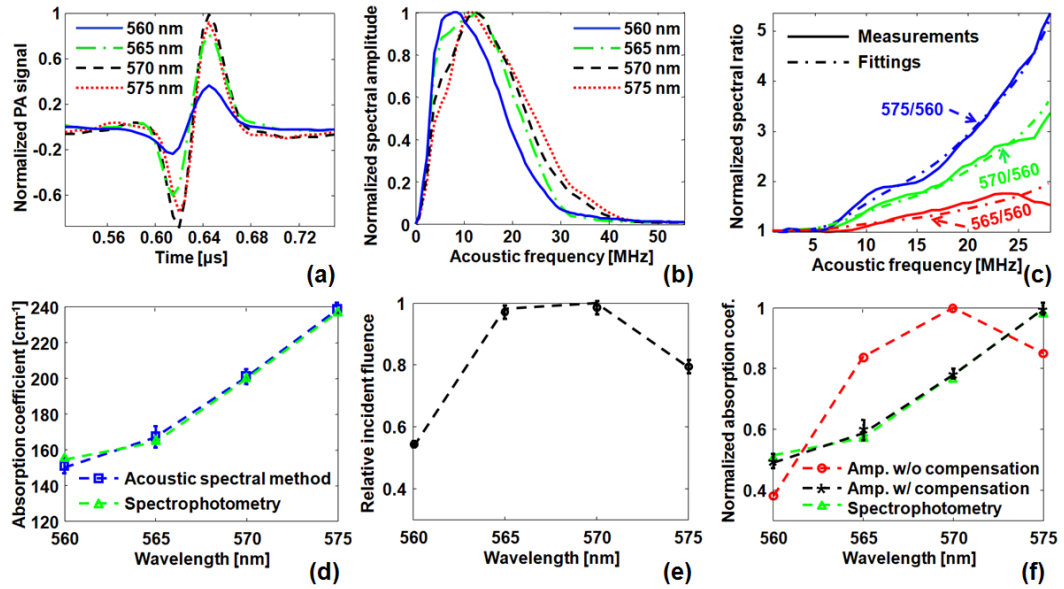


**Figure 2.5 Quantification of the optical absorption coefficients of oxygenated bovine blood phantom.** (a) PA time domain A-scan signals of the oxygenated-bovine-blood-filled tube phantom buried in the scattering medium. (b) Acoustic spectra of the PA A-scan signals. (c) Acoustic spectral ratios and fittings with the theoretical formula. (d) Comparison of the optical absorption coefficients quantified with the acoustic spectral method and measured by spectrophotometry. (e) Relative incident fluence quantified with the acoustic spectral method. (f) Comparison of the relative optical absorption coefficients quantified from the PA signal amplitudes with and without the fluence compensation and measured by spectrophotometry. Amp.: the amplitude method with and without the fluence compensation.

In the phantom study, PA A-line signals at four wavelengths were acquired from the samples [Fig. 2.5(a)] and were normalized to the peak of the PA signal measured at 570 nm. The corresponding acoustic spectra of the PA signals [ $S(\omega, \lambda)$ ] were calculated [Fig. 2.5(b)]. Light penetrated deeper at longer wavelengths, and the corresponding PA signals decayed more slowly in the time domain. As the wavelengths increased, the fluence decayed faster in the tube, and the produced PA signals were sharper with time.

Therefore, the acoustic spectra acquired at longer optical wavelengths contained more high-frequency components. By dividing the measured spectra from any two wavelengths, frequency by frequency [Fig. 2.5(c)], we found the absorption coefficients at both wavelengths as well as the relative incident fluence by fitting the resultant spectral ratio curve. In comparison to the gold-standard—spectrophotometry, the acoustic spectral method quantified the absorption coefficients with relative errors of 1%, 3%, 1.2%, and 1.5% at the optical wavelengths of 560, 565, 570, and 575 nm, respectively [Fig. 2.5(d)], where the error bars indicate the fitting standard errors. From the quantified incident fluence ratios at all the wavelength pairs, we obtained the relative incident fluence at each of the four wavelengths by normalizing to the maximum incident fluence at 570 nm [Fig. 2.5(e)]. Normalizing the PA signal amplitude at each wavelength by the corresponding relative incident fluence yields the relative optical absorption coefficient [Fig. 2.5(f)]. This normalization process is referred to as fluence compensation, because it calibrates the wavelength-dependent fluence attenuation. In contrast, quantifying the absorption coefficients from the PA signal amplitudes without the fluence compensation is inaccurate [Fig. 2.5(f)].

### 2.3.3 *In Vivo* Studies

In an *in vivo* experiment, we imaged an 8 mm by 8 mm region of the back of a nude mouse with two optical wavelengths (571 nm and 564 nm). Next, an optical phantom layer ( $\sim 1.5$  mm of 10% gelatin, 1% intralipid, 5%  $\text{CuCl}_2$ ) was used to cover the back of the nude mouse, and the same region was imaged again.

Figures 2.6(a) and 2.6(b) show the PA maximum amplitude projection (MAP) images, in which each point corresponds to the maximum value of a Hilbert transformed PA A-scan. Since these blood vessels are shallow [ $\sim 150$   $\mu\text{m}$  deep, as shown in Fig. 2.6(c)], the effect of wavelength-dependent fluence attenuation is negligible. We obtained the  $\text{sO}_2$  and [HbT] control images [Figs. 2.6(d) and 2.6(e)] based on Eq. (2.3) from the PA signal amplitudes. From the  $\text{sO}_2$  image, the arteries and the veins can be clearly identified [Fig.

2.6(d)]. Figures 2.6(f) and 2.6(g) show the PA MAP images of the same region with the optical phantom layer, where the blood vessels are  $\sim 1.6$  mm deep [Fig. 2.6(h)]. In this case, if we ignored the wavelength-dependent fluence variations induced by the optical phantom layer, the  $sO_2$  quantified from the amplitudes of the PA signals [Fig. 2.6(i)] became inaccurate by approximately 32%. The average quantification error of the relative [HbT] [Fig. 2.6(j)], however, was only 5%, because the blood vessels in the FOV was located approximately at the same depth [Fig. 2.6(h)]; thus, the fluence attenuation effect was eliminated by the normalization process. Nevertheless, the amplitude method provides only relative quantifications.

Since the light was completely diffused by the optical phantom layer and the blood vessel diameters were much larger than the imaging resolution, the assumptions in our acoustic spectral method were valid. For each scanning position, we divided, frequency by frequency, the acoustic spectrum measured at 564 nm by the acoustic spectrum measured at 571 nm. The optical absorption coefficients [Figs. 2.6(k) and 2.6(l)] as well as the relative incident fluence [Fig. 2.6(m)] were acquired by fitting the spectral ratios defined by Eq. (2.9). Then the  $sO_2$  and [HbT] images [Figs. 2.6(n) and 2.6(o)] were quantified from the absolute optical absorption coefficients. By comparing the quantification results to the control images, we found the acoustic spectral method achieved average errors of 7% and 6% in quantifying  $sO_2$  and [HbT], respectively. Here, we normalized [HbT] by the maximum to make a fair comparison. Normalizing the amplitudes of the MAP PA images at two wavelengths by the corresponding relative incident fluences yields the relative optical absorption coefficients. Specifically, the PA MAP image at 571 nm [Fig. 2.6(f)] is divided by 1, while the PA MAP image at 564 nm [Fig. 2.6(g)] is divided, point by point, by the relative incident fluence [Fig. 2.6(m)]. After the fluence compensation, the  $sO_2$  [Fig. 2.6(p)] and the relative [HbT] [Fig. 2.6(q)] were quantified from the calibrated PA amplitudes with average errors of 9% and 5%.

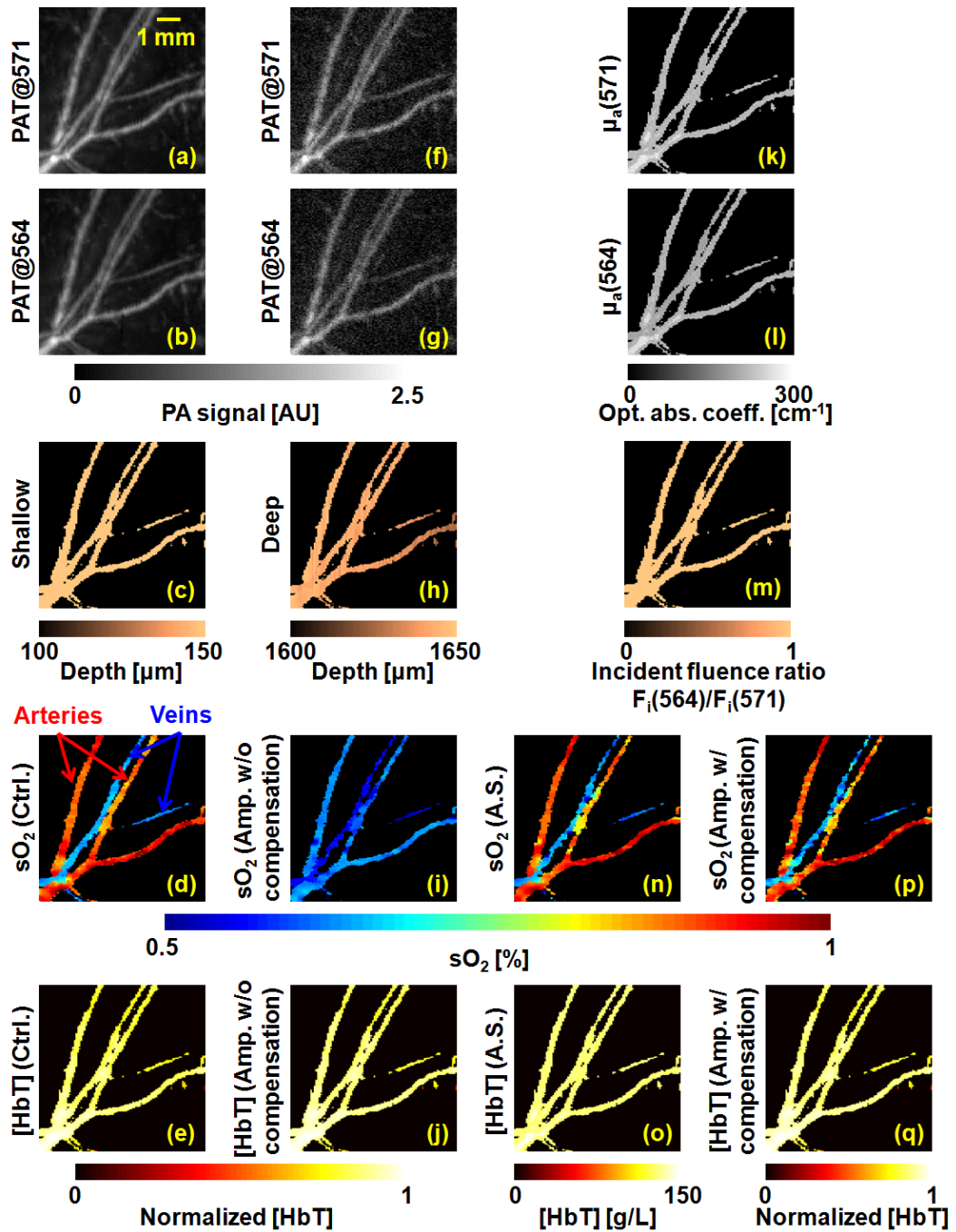


Figure 2.6 Quantification of the  $sO_2$  and  $[HbT]$  of blood vessels in the back of a nude mouse *in vivo*. MAP image acquired at (a) 571 nm and (b) 564 nm. (c) Depth-encoded image of blood vessels. (d) Control images of  $sO_2$  and (e)  $[HbT]$ . MAP image acquired with an optical phantom layer at (f) 571 nm and (g) 564 nm. (h) Depth-



encoded image of blood vessels below the optical phantom layer. (i) sO<sub>2</sub> and (j) [HbT] quantified from the amplitude method. Absolute optical absorption coefficients at (k) 571 nm and (l) 564 nm and (m) relative incident fluence quantified with the acoustic spectral method. (n) sO<sub>2</sub> and (o) [HbT] quantified from the absolute optical absorption coefficients. (p) sO<sub>2</sub> and (q) [HbT] quantified from amplitude method with the fluence compensation. Amp.: the amplitude method with and without the fluence compensation. A.S.: the acoustic spectral method. Ctrl.: the control image.

### 2.3.4 Discussion

We have proposed a method to quantify [HbT] and sO<sub>2</sub> *in vivo* using acoustic spectra of PA signals from multiple optical wavelength measurements. The optical and acoustic effects that affect the quantification accuracy have been eliminated. Using AR-PAM, we first demonstrated this method with phantom experiments and then quantified the [HbT] and sO<sub>2</sub> in a live mouse. The acoustic spectral method provides greater quantification accuracy than the conventional amplitude method in the optical diffusive regime. This method can potentially be applied to all other reflection- or transmission-mode PAT setups.

# Chapter 3

## Compressed Sensing in PAT

### 3.1 Under-sampling in PAT

Reliable image reconstruction with sparse sampling of the detecting aperture is desirable. In practical PAT systems, it is recommended [27, 36] to set the discrete spatial sampling period to be two to five times smaller than the sensing aperture of the detector. For a scanning PAT system, it may require hundreds or even thousands of scanning steps to acquire an image, depending on the sizes of both the detector and the detecting aperture. Such scanning usually takes several minutes to complete. To reach real-time imaging, PAT is implemented with an array of ultrasonic transducers, where all or groups of the array elements can detect photoacoustic signals simultaneously. However, the data acquisition speed is still limited by the number of parallel data acquisition (DAQ) channels, and employing a large number of DAQ channels greatly increases the system cost. For example, for a fast 512-element ring array PAT system with a 64 channel data acquisition module [37], it takes 8 laser shots to collect data from all 512 elements. For direct 3-D reconstruction PAT applications [38, 39], the data from a 2-D ultrasonic array is usually an extremely sparse sampling of the detecting aperture. Moreover, channel crosstalk is also related to the space between neighboring elements (kerf), and an extensive spatial sampling may increase the crosstalk.

Imaging an object in PAT can be understood as sensing the object in a certain domain. For example, with the ‘Fourier-shell identity’ [54], PAT can also be seen as detecting the spatial frequencies of the object (sensing in the Fourier domain). Sparse spatial sampling of the detection aperture implies that the spatial frequencies cannot be exactly determined. Traditional backprojection (BP) reconstruction methods [55] reconstructs the image of “minimal energy” under the observation constraints. An improved reconstruction algorithm should be able to “guess” these undetermined frequency components. However, interpolation in the Fourier domain is a critical issue, and usually creates artifacts in reconstructed images [56]. The recently developed compressed sensing (CS) theory [57] enables us to recover these unobserved components under certain conditions. The theory has been successfully applied in MRI [58], where MRI images were able to be reconstructed from significantly undersampled K-space measurements. Paper [59] introduced the CS theory into the field of PAT, and the idea was tested in phantoms using a circular scanning PAT system. In this chapter, we improve the speed of the reconstruction algorithm by adopting a non-linear conjugate gradient descent method, and demonstrate the algorithm with both phantom and animal data, using various detecting geometries.

## **3.2 Application of the Compressed Sensing Theory in PAT**

### **3.2.1 The Forward and the Inverse Problems in PAT**

In PAT, pulsed laser irradiation creates pressure rises as a result of thermoelastic expansion. These initial pressure rises propagate as photoacoustic waves, which can be detected by ultrasonic sensors. Based on the pressure measurements  $p(\vec{r}, t)$  at the detecting aperture, PAT reconstructs the image of the initial pressure rise distribution

$p_0(\bar{r})$ . The forward and inverse problems in PAT express the reciprocal relationship between  $p_0(\bar{r})$  and  $p(\bar{r}, t)$ . By solving the wave equation, the forward problem, which predicts  $p(\bar{r}, t)$  by  $p_0(\bar{r})$ , can be derived as (assuming a delta pulse heating):

$$p(\bar{r}, t) = \frac{\partial}{\partial t} \left[ \frac{1}{4\pi c^3 t} \int d\bar{r}' p_0(\bar{r}') \delta \left( t - \frac{|\bar{r} - \bar{r}'|}{c} \right) \right], \quad (3.1)$$

where  $c$  is the speed of ultrasound and  $\bar{r}$  is the position of the ultrasonic sensor [6]. Sometimes the velocity potential  $\varphi(\bar{r}, t) = \int_0^t p(\bar{r}, t') dt'$  is employed to simplify Eq. (3.1):

$$\varphi(\bar{r}, t) = \frac{1}{4\pi c^3 t} \int d\bar{r}' p_0(\bar{r}') \delta \left( t - \frac{|\bar{r} - \bar{r}'|}{c} \right).$$

The analytical inversion of Eq. (3.1) describes the inverse problem, which reconstructs  $p_0(\bar{r})$  with  $p(\bar{r}, t)$ :

$$p_0(\bar{r}) = \int_{S_0} \left[ 2p(\bar{r}_0, \bar{t}) - 2\bar{t} \partial p(\bar{r}_0, \bar{t}) / \partial \bar{t} \right] \Big|_{\bar{t}=|\bar{r}-\bar{r}_0|} d\Omega_0 / \Omega_0, \quad (3.2)$$

where  $\bar{t} = ct$ ,  $S_0$  is the detecting aperture, and  $d\Omega_0 / \Omega_0$  is the solid-angle weighting factor.

To numerically model the forward and inverse problems, we need to properly discretize Eqs. (3.1) and (3.2). We use a vector  $x$  to represent  $p_0(\bar{r})$ , where each element of  $x$  is the average value of initial pressure per unit volume. The size of  $x$  ( $N_x \times N_y \times N_z$ ) depends on the field of view (FOV) and the desired spatial resolution of the reconstructed image. We use a vector  $y$  to denote the velocity potential  $\varphi(\bar{r}, t)$  measured by all elements of the sensor array as a function of time. The size of  $y$  is the number of detecting positions ( $L$ ) times the number of temporal samples at each position ( $M$ ). Then, the forward problem can be described as  $y = \Phi x$ , where matrix  $\Phi$  is the projection matrix. Similarly, the inverse problem can be written as  $\bar{x} = \Phi^{-1} y$ , where  $\Phi^{-1}$  represents the inverse process and  $\bar{x}$  is the reconstructed image.

$\Phi$  and  $\Phi^{-1}$  are usually extremely large matrices (each containing  $N_x \times N_y \times N_z \times L \times M$  data points), even for 2-D reconstruction problems. For example, when reconstructing a  $256 \times 256$  image with measurements from 512 detecting positions, where each position has 1024 time points, both  $\Phi$  and  $\Phi^{-1}$  contain  $3.436 \times 10^{10}$  data points ( $\sim 256$  GB if each point is expressed in double-precision), which makes direct matrix operations computationally impractical. Paper [60] tried to solve this problem by saving only non-zero elements of metrics  $\Phi$  and  $\Phi^{-1}$ . For each detecting element  $i$  ( $i = 1, 2 \dots L$ ), the forward and inverse operations are performed using a matrix of the same size as  $x$ . Each element in this matrix stores an index of the temporal sample ( $k = 1, 2 \dots M$ ) of measurement  $i$ , and this index indicates where the corresponding element of  $x$  should be projected. As a result, the storage space for both the forward and inverse operations for all elements is reduced to  $N_x \times N_y \times N_z \times L$  ( $\sim 256$  MB for the above example). To fully take advantage of parallel computing capability, the responses of all the elements can be calculated simultaneously.

### 3.2.2 Sparsity and Incoherence

If the measurement is incomplete, matrix  $\Phi$  is ill-conditioned, and  $\Phi^{-1}$  is obviously not an exact inversion of  $\Phi$ . Intuitively, an incomplete dataset usually leads to uncertainties in the recovery of the signals. In the case of PAT reconstruction with insufficient measurements, the BP method usually generates streaking artifacts or grating lobes. However, these uncertainties can be eliminated by incorporating prior information, such as sparsity constraints. The CS theory was rigorously formulated to reconstruct images from incomplete datasets. To make this possible, the CS theory relies on two principles: sparsity, which pertains to the object of interest, and incoherence, which pertains to the sensing modality. Moreover, a non-linear reconstruction is used to enforce both sparsity of the image representation and consistency with the acquired data.

Unlike ultrasound imaging and all other coherent imaging technologies, PAT is devoid of speckle artifacts and sensitive to boundaries because of its optical absorption contrast [51]. Therefore, computing the Finite Difference (FD) of PAT images in the spatial domain sometimes directly results in a sparse representation. When imaging objects with rich absorbing structures such as blood vessels in the mouse brain cortex, however, PAT images may not be sparse in the spatial domain. In these cases, we need to project the images onto an appropriate basis set, such as the wavelet basis. Mathematically speaking, if we use a vector  $x \in R^n$  to represent an  $n$ -pixel image and  $\Psi$  to denote the wavelet basis set, then  $x$  can be expanded as  $x = \sum_{i=1}^n a_i \psi_i$ , where  $a_i = \langle x, \psi_i \rangle$  is the coefficient sequence of  $x$ . Even when most of the image pixels have nonzero values, the wavelet coefficients may provide a concise representation of the original image: most coefficients are small, and the relatively few large coefficients capture most of the information. The speckle-free nature [51] of PAT images further reduces the number of significant transform coefficients.

Since the object  $x$  can be visually losslessly reconstructed with only a few large transform coefficients, the problem of sensing  $x$  is equivalent to capturing these large coefficients in the representation domain  $\Psi$ . The forward problem of PAT can be seen as projecting the object  $x$  to the sensing basis set  $\Phi$ , and the measurements are the resulting coefficients. The CS theory requires the two basis sets  $\Psi$  and  $\Phi$  to be incoherent, i.e., the sensing waveforms should have a dense representation in  $\Psi$ . In other words, the undersampled sensing basis  $\Phi$  should only induce incoherent artifacts that spread out and appear as random noise in  $\Psi$ .

It is difficult to mathematically demonstrate that a physical system satisfies the incoherence condition. The Transform Point Spread Function (TPSF) [58, 59] was introduced to measure incoherence. Figure 3.1 illustrates the definition of TPSF in PAT. A wavelet transform is adopted as the sparsifying transform  $\Psi$ , and we assume that a circular detecting aperture is uniformly sampled by multiple ultrasonic point

sensors. The  $i$ th transform coefficient  $e_i$  in the domain  $\Psi$  [Fig. 3.1(a)] is transformed to the image space [Fig. 3.1(b)] by the inverse discrete wavelet transform (IDWT). Then the measurements are generated with the forward operator  $\Phi$ , and transformed back to the image space [Fig. 3.1(c)] with the inverse operator  $\Phi^{-1}$ . Finally the reconstructed image is again transformed to the sparse domain  $\Psi$  [Fig. 3.1(d)] with the forward discrete wavelet transform (FDWT).

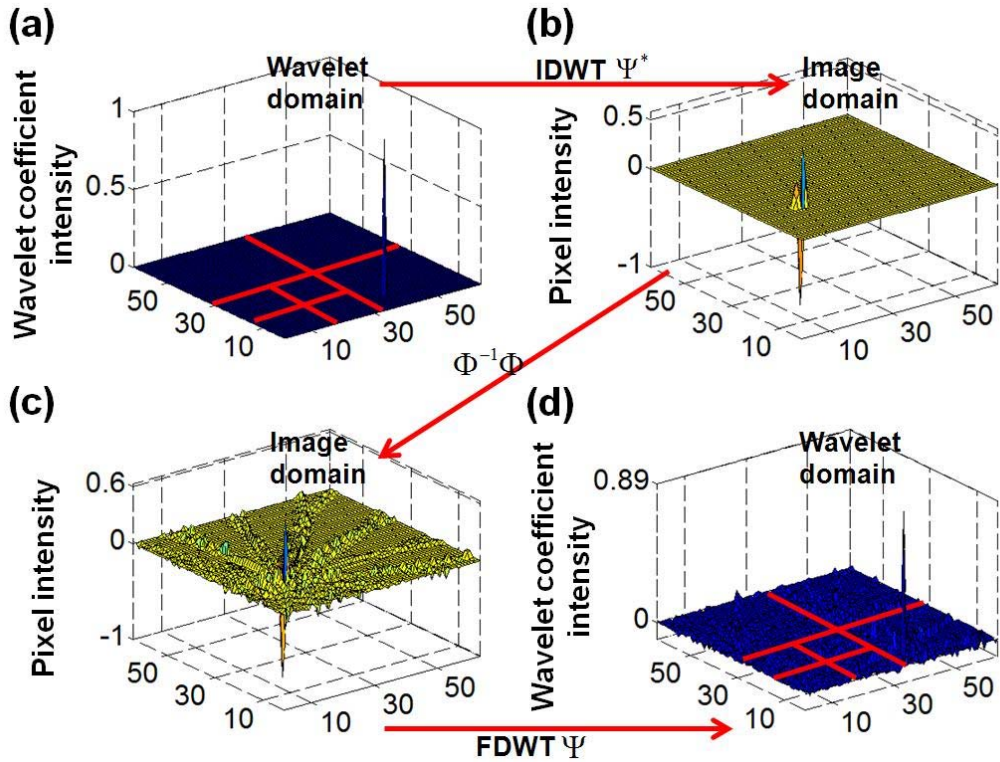


**Figure 3.1 Illustration of the wavelet TPSF.** (a) A wavelet coefficient of unit intensity; (b) IDWT of (a) in the image domain; (c) Sensing (b) with 16 ultrasonic sensors and reconstructed with the BP method; (d) FDWT of (c).

TPSF can be mathematically described as  $TPSF(i, j) = e_j^* \Psi \Phi^{-1} \Phi \Psi^* e_i$ , and it measures the leakage of energy away from the  $i$ th coefficient to other coefficients. The CS theory requires us to properly choose  $\Phi$  and  $\Psi$  so that these interferences can be minimized

and spread out in  $\Psi$ . Readers are referred to paper [59] for a quantitative comparison of the TPSF maps for various  $\Psi$  in PAT.

### 3.2.3 Reconstruction Method

If it satisfies the above two conditions, a sparse signal can be accurately recovered from highly incomplete datasets by solving a non-linear convex optimization problem. We now describe in more detail the CS reconstruction method for PAT. In the CS theory, the reconstruction of image  $x$  is obtained by solving the following constrained optimization problem:

$$\min_x |\Psi x|_1 \quad \text{s.t.} \quad |\Phi x - y|_2 < \varepsilon. \quad (3.3)$$

Here  $\Psi$  and  $\Phi$  are defined as above,  $y$  is the measured data, and  $\varepsilon$  is the parameter that controls the fidelity of the reconstruction to  $y$ . The parameter  $\varepsilon$  is usually set based on the expected noise level. The object function in Eq. (3.3) is the  $l_1$  norm (defined as  $|x|_1 = \sum |x_i|$ ). The  $l_1$  norm is used here instead of the  $l_2$  norm (defined as  $|x|_2 = \sqrt{\sum |x_i|^2}$ ), because the  $l_2$  norm penalizes large coefficients heavily, and leads to non-sparsity. In the  $l_1$  norm, many small coefficients tend to carry a much larger penalty than a few large coefficients, therefore small coefficients are suppressed and solutions are often sparse. In Eq. (3.3), minimizing the  $l_1$  norm of  $\Psi x$  promotes sparsity, and the constraint enforces data consistency.

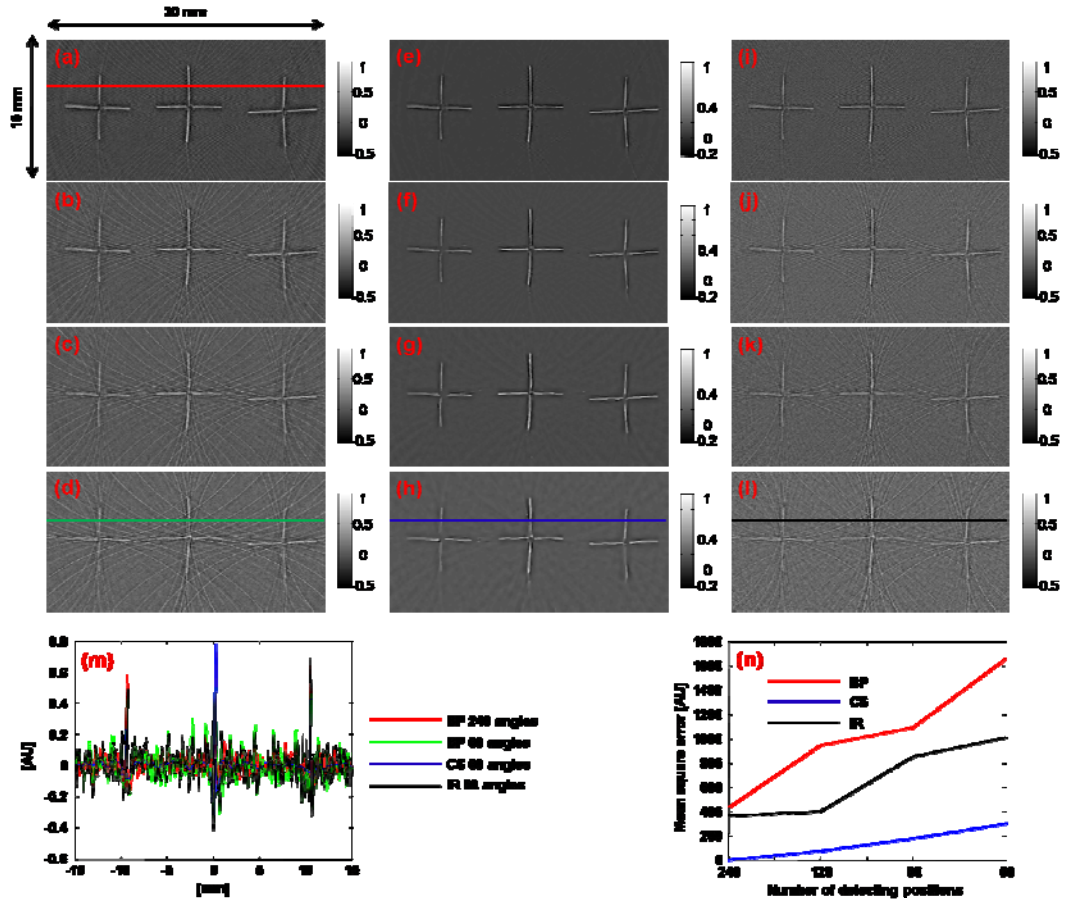
The algorithm is implemented with a non-linear conjugate gradient descent method [61], as detailed in the Appendix C. On a laptop with a dual-core 2-GHz CPU and 3-GB memory, the calculations usually take less than 10 minutes using Matlab 2008a.



### 3.3 Results and Discussions

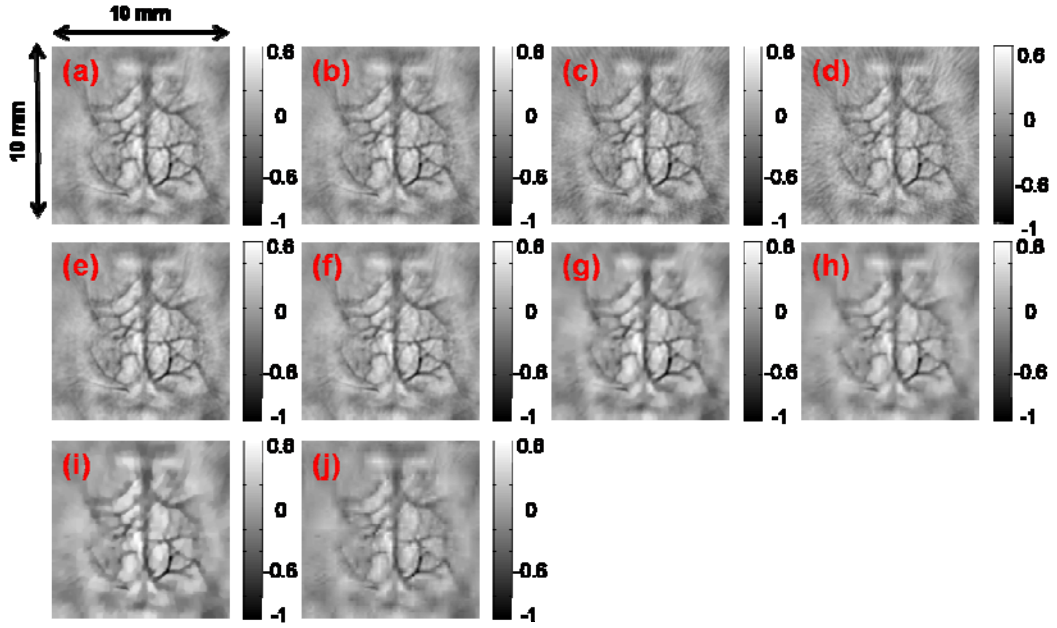
We first demonstrate the CS method using a tissue mimicking phantom experiment. Tissue phantoms were imaged by scanning a virtual point detector in a setup similar to that of [62]. The PA source contained three black human hair crosses glued on top of optical fibers, with an interval between the hair crosses of about 10 mm. Laser pulses with a repetition rate of 10 Hz were diverged by a ground glass to achieve a relatively uniform illumination. The virtual point detectors evenly scanned the object along a horizontal circle, stopping at 240 points, and the signals were averaged over 20 times at each stop. The total data acquisition time was 8 minutes.

Figure 3.2 shows the reconstruction results with the BP [Figs. 3.2(a)–3.2(d)], the CS [Figs. 3.2(e)–3.2(h)], and the traditional iterative [60] (IR) [Figs. 3.2(i)–3.2(l)] methods, with 240, 120, 80, and 60 tomographic angles. The images are reconstructed with a FOV of 30 mm×15 mm. We can observe that the CS method is clearly superior to the BP and the IR methods. This can be shown by extracting and comparing lines from the reconstructed images [Fig. 3.2(m)]. The interference level has been reduced significantly with the CS reconstruction. Moreover, as predicted by the theory, the CS scheme is robust to inaccurate measurements, so the noise level has also been suppressed. We took Fig. 3.2(e) as the gold standard, and calculated the mean square errors (MSE) of all other images from the standard, as shown in Fig. 3.2(n). Using the CS reconstruction method, we improved the data acquisition time in the circular scanning geometry by fourfold.



**Figure 3.2 Tissue phantom imaging with a virtual point detector.** (a)–(d) Images reconstructed using the BP method with 240, 120, 80, and 60 tomographic angles; (e)–(h) Images reconstructed using the CS method with 240, 120, 80, and 60 tomographic angles; (i)–(l) Images reconstructed using the traditional iterative reconstruction method with 240, 120, 80, and 60 tomographic angles; (m) Lines extracted from (a), (d), (h), and (l); (n) Comparison of the mean square errors of the three reconstruction methods.

The first *in vivo* experiment was based on a custom designed 512-element photoacoustic tomography array system [37]. The 5 MHz piezocomposite transducer array was formed into a complete circular aperture. With a 64-channel data acquisition module, the system could provide full tomographic imaging at up to 8 frames/second. We used this system to image mouse cortical blood vessels.



**Figure 3.3** *In vivo* imaging of the mouse cortex with a circular ultrasonic array.

(a) – (d) Images reconstructed using the BP method with 512, 256, 171, and 128 detecting elements; (e) – (h) Images reconstructed using the CS method with 512, 256, 171, and 128 detecting elements; (i) Images reconstructed using the CS method with 128 detecting elements and with only the TV regularization; (j) Images reconstructed using the CS method with 128 detecting elements and with only the wavelet regularization.

The images were reconstructed by the BP [Figs. 3.3(a)–3.3(d)] and the CS [Figs. 3.3(e)–3.3(h)] algorithms, with 512, 256, 171, and 128 detecting elements, respectively. To achieve the optimal reconstruction results, we simultaneously used both the total variance (TV) and the wavelet as sparsifying transforms in the CS method. The undersampling artifacts appear in the outer region in Fig. 3.3(h), which is a natural result of the spatial variant PSF in PAT. Figure 3.3(i) shows the images reconstructed with 128 tomographic angles using only the TV regularization, which promotes sharp boundary features and suppresses small variances. Figure 3.3(j) shows the images reconstructed using only the wavelet regularization, and the image is “blurred”. Since 128 tomographic angles does not contain enough information to capture all the important transform

coefficients, the reconstruction artifacts started to appear and some object features started to disappear.

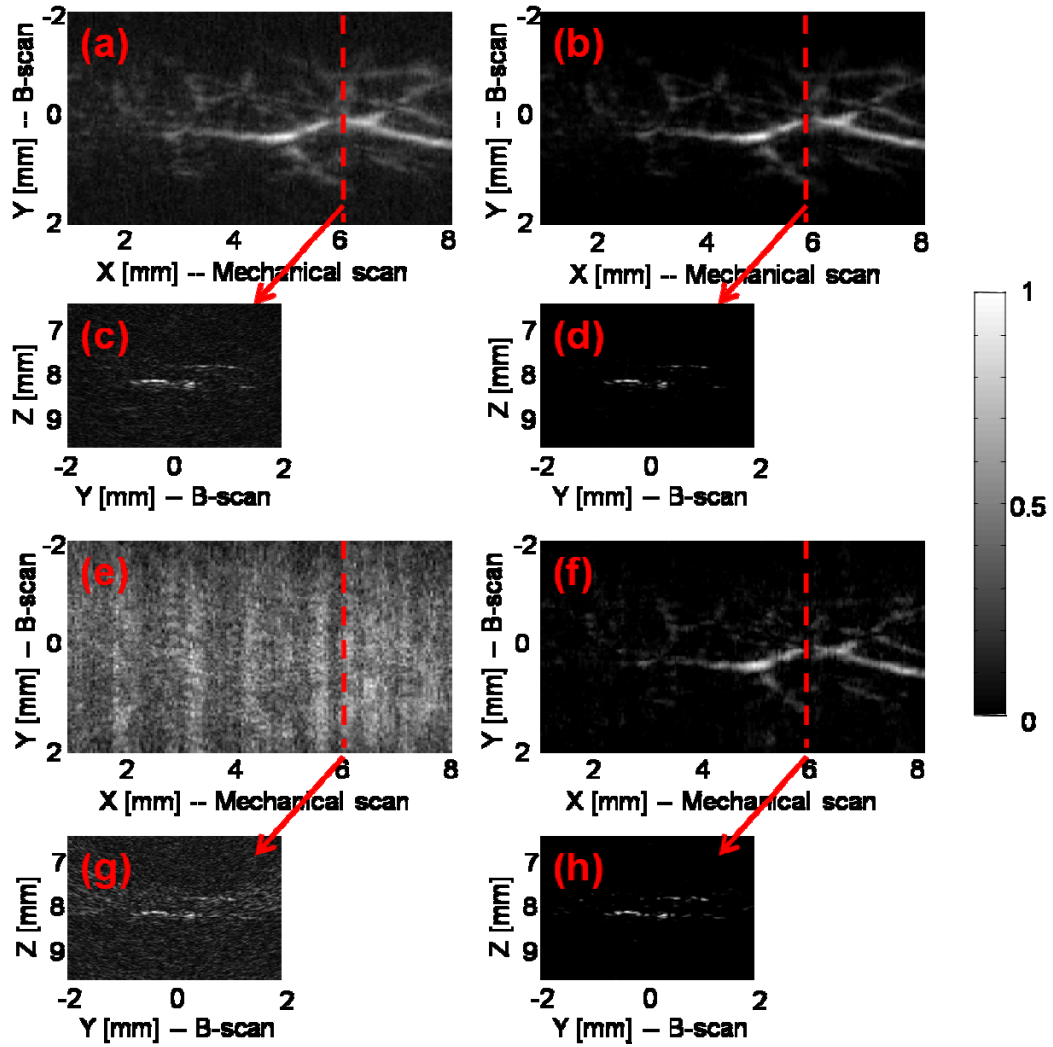


Figure 3.4 *In vivo* imaging of the upper dorsal region of a rat with a linear array. (a), (b) MAP images reconstructed using 48 elements with the BP and the CS methods, respectively; (c), (d) typical B-scans extracted from (a), (b); (e), (f) MAP images reconstructed using 16 elements with the BP and the CS methods, respectively; (g), (h) typical B-scans extracted from (e), (f).

The second *in vivo* experiment demonstrates the capability of the CS method with linear array detecting geometry. The 30 MHz broadband linear transducer array has a total of 48 elements of dimensions  $82 \mu\text{m} \times 2 \text{ mm}$  with  $100 \mu\text{m}$  pitch [63]. The linear array is focused in the elevation direction to perform cross-sectional (B-scan) imaging, and 3-D volume imaging can be achieved by scanning the probe in the third dimension. We scanned the upper dorsal region of a rat to image the subcutaneous vasculature, and acquired a total of 166 B-scan slices. Each B-scan image was reconstructed with both the BP and the CS methods, and the Hilbert transform was taken after the reconstruction. After processing all the B-scans, the maximum amplitude projection (MAP) images were acquired through projecting the B-scans along the axial direction. Figures 3.4(a) and 3.4(b) show MAP images reconstructed with the BP and the CS methods, respectively, and one typical B-scan was extracted as shown in Figs. 3.4(c) and 3.4(d). We observed a significantly reduced noise level with the CS reconstruction. To further demonstrate the ability of CS method in reducing the undersampling artifacts, we aggressively reconstruct the image with only 16 elements (1/3 of total 48 elements) with both the BP and the CS method. The results are shown in Figs. 3.4(e)–3.4(h). With the BP reconstructions, the extremely sparse linear array generates significant grating lobe artifacts. By comparison, these under-sampling artifacts were effectively reduced with the CS reconstruction.

Both the phantom and the *in vivo* results show that the CS method can effectively reduce the undersampling artifacts. By incorporating the CS theory in the PAT reconstruction, we can effectively reduce the system cost, or cover a larger FOV with the same number of measurements. Although the CS method is only demonstrated here with 2D problems, the generalization to 3D reconstructions is straight forward.

# Chapter 4

## Speckles in PAT

### 4.1 On the Speckle-free Nature of PAT

Speckles have been considered ubiquitous in all scattering-based coherent imaging technologies. As a coherent imaging modality based on optical absorption, photoacoustic (PA) tomography (PAT) is generally devoid of speckles. In section 4.1, we explain the inherent mechanism that suppresses speckle in PAT [64].

Currently, PAT has been implemented in two major forms [11]. One is focused-scanning PAT such as photoacoustic microscopy (PAM). One-dimensional depth-resolved photoacoustic images (A-scans) are collected by scanning a focused ultrasonic transducer. A cross-sectional or volumetric image is composed by aligning multiple A-scans at the corresponding lateral positions. The other form of implementation is photoacoustic computed tomography, in which an array of unfocused ultrasonic transducers is placed outside the object, and an image is formed using reconstruction algorithms. The following discussion in section 4.1 is based on a reflection-mode focused-scanning PAT system developed in our laboratory, where a 5 MHz focused ultrasonic transducer is employed [65]. However, the linearity of PAT guarantees that the principles discussed here hold for all PAT variants.

### 4.1.1 Intuitive Explanation

When researchers analyze the speckle statistics in ultrasound imaging, a scattering structure is usually modeled as a collection of randomly distributed sub-resolution scatterers. The ultrasonic waves scattered from these scatterers interfere with each other, and speckles are formed.

In PAT, an optically absorbing structure can be modeled as a collection of randomly distributed sub-resolution absorbers. The absorbers can vary in dimension widely, from hemoglobin molecules to red blood cells, as long as they are much smaller than the spatial resolution and are randomly distributed in the resolution cell. The axial resolution of the 5 MHz PAT system, limited by the transducer bandwidth, is  $\sim 144 \mu\text{m}$ . The lateral resolution, determined by the width of the focal spot, is  $\sim 560 \mu\text{m}$ . Because an average adult has  $\sim 5$  million red blood cells ( $\sim 7.4\text{--}9.4 \mu\text{m}$  in diameter and  $\sim 1.6\text{--}2.0 \mu\text{m}$  in thickness) per microliter of blood, the ultrasonic transducer may receive photoacoustic waves from  $\sim 5.8 \times 10^4$  red blood cells within a resolution cell. The photoacoustic signals emitted from these absorbers interfere with each other. Curiously, investigators have noticed that photoacoustic methods, despite their coherent nature, produce images devoid of speckle artifacts. We found that this salient feature is a direct result of the absorption contrast in PAT.

As the first explanation of the speckle-free nature of PAT, we compare a pulse-echo ultrasound imaging system with the 5 MHz reflection-mode PAT system. Both systems can be described by the same linear model. For a fair comparison without loss of generality, the same spatial-temporal system impulse response  $h(\vec{r}, t)$  is assumed for both systems. In reality,  $h(\vec{r}, t)$  in pulse-echo ultrasonography represents a round trip response, while  $h(\vec{r}, t)$  in PAT represents only one way.

Figure 4.1 shows that a focused ultrasonic transducer detects A-scan signals from a slab of tissue. The tissue slab is modeled as a collection of randomly distributed particles (red

dots), which can be either acoustic scatterers in ultrasound imaging or optical absorbers in PAT. For simplicity, we consider the particles as point targets because they are small relative to the spatial resolution.

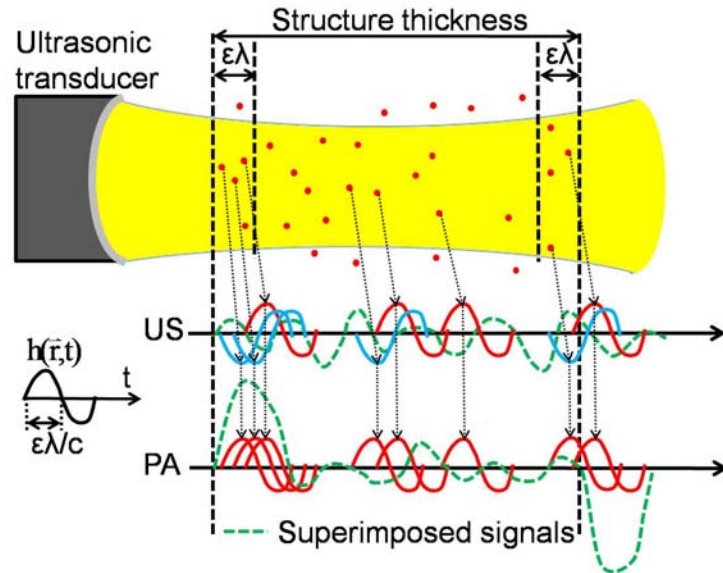


**Figure 4.1 Comparison of pulse-echo ultrasound imaging and reflection-mode PAT.** A focused ultrasonic transducer records the A-scan signal from a slab.  $\epsilon\lambda$ : a fraction of the central acoustic wavelength  $\lambda$ ;  $c$ : speed of ultrasound. PA: Photoacoustic; US: Ultrasound.

In the ultrasonic A-scan, the received signals from the individual scatterers may either maintain (red solid curves) or flip (blue dotted curves) the polarity of  $h(\vec{r}, t)$ , because the acoustic impedance of the scatterers may be either lower or higher than the surrounding medium. The photoacoustic A-scan from the absorbers of the same geometry is also plotted. Because all initial pressure rises are positive, all received photoacoustic waves uphold the polarity of  $h(\vec{r}, t)$ , which is the major difference between PAT and ultrasound imaging. The A-scan signals, plotted in green dashed lines, result from the interference among the signals from the individual particles. In the middle segment of the A-scan signals in both imaging modalities, we observe random fluctuations, because of the cancellation among the positive and negative parts of



$h(\vec{r}, t)$ . Further, the mean of the amplitudes of the fluctuations are zero because  $h(\vec{r}, t)$  does not contain a DC component. In the cases when very wideband acoustic sensors that can detect DC component are employed in PAT, we expect to see not only the boundary buildups, but also the baselines inside the object. Near both the front and back boundaries, however, prominent boundary signals are observed in the photoacoustic A-scan, because of the constructive interferences. As a result, the random fluctuations in the middle are suppressed by the boundary signals, which we found to be the dominant features in photoacoustic images. By contrast, the boundary signals in ultrasound images do not stand out because of the existence of both scattering polarities. Therefore, speckle appears ubiquitously in ultrasonic A-scans.

#### 4.1.2 Classic Speckle Theory Explanation

As the second explanation, the classic speckle theory is invoked. As stated above, the fully developed speckle is formed by the interference of coherent waves with completely randomized phases. Two components contribute to the phase difference between waves: the initial phase and the phase delay. When profiling the central part of the structure in both photoacoustic and ultrasound imaging, we always receive acoustic waves from particles with completely randomized phases, which result from phase-delay variations. However, particles close to the boundaries send out waves that reach the transducer with approximately equal phase delays. Here, the initial phase plays a key role. As the initial photoacoustic pressure rises are always positive, the emitted photoacoustic waves add constructively to manifest the boundaries. By contrast, the scattered ultrasonic waves can take on both positive and negative initial phases. Hence, no boundary buildups are observed.

However, speckles in scattering-based coherent imaging modalities are under-developed in some circumstances. For example, if mirror surfaces are imaged by optical coherence tomography, or smooth bone surfaces are imaged by ultrasonography, we observe a phenomenon referred to as ‘specular reflection’ [44]. Specular reflection is formed by

constructive interference of coherent partial waves that have phases randomized only within  $[0, \pi]$  or less. For scattering-based coherent imaging, two conditions must be met to ensure specular reflection. First, all scatterers on the surface must have similar properties so that the polarity changes to the incident wave due to backscattering are the same. Second, the boundary roughness must be less than  $\lambda/4$ —with  $\lambda$  being the center wavelength—so that the phase-delay variations due to scatterer spatial distribution differences are within  $\pi$ .

In fact, PAT suppresses speckles by building up prominent boundary, referred to as “specular emission” here, via a mechanism similar to that of specular reflection. First, because the initial PA pressure rise is always positive, the propagated PA wave from any finite-sized optical absorber starts with a positive pressure and ends with a negative pressure [66]. In addition, because most PAT systems are linear and shift-invariant, the changes to the polarities of these partial waves due to imaging systems are the same. As a result, these partial waves possess the same initial polarities. Therefore, PAT naturally satisfies the first condition for “specular reflection” except that “specular emission” is a more accurate description. Second, the optical absorbing targets in biological tissues, such as blood vessels, usually have smooth surfaces on the scale of the wavelengths of megahertz ultrasonic waves. Thus, the PA partial waves from most surface absorbers are generated within a region of  $\lambda/2$  in thickness at the boundary of the absorbing target, yielding phase-delay variations within  $\pi$ . Consequently, the second condition for specular emission is also satisfied, and the constructive interference among the partial waves from individual absorbers leads to boundary buildups. By contrast, the PA partial waves generated from the interior of a sufficiently large absorbing target have phase-delays randomized over a full range of  $2\pi$ . Therefore, the second condition for specular emission is violated, and speckles are formed from the interior of the absorbing targets.

The second condition for specular emission is violated in rare cases, which will be discussed in section 4.2.

### 4.1.3 Mathematical Explanation

As the third explanation, we analyze the condition for building up boundaries in all coherent imaging modalities and compare the strengths of the boundaries and of the interior speckle in PAT quantitatively. Assume that a total of  $n$  particles (absorber or scatterer) are statistically uniformly distributed at positions  $\bar{r}_1, \bar{r}_2 \dots \bar{r}_n$ . We use random process  $a_i(t)$  to denote the particle impulse response, which accounts for the properties of a single particle. Because PAT is based on the optical absorption contrast,  $a_i(t)$  depends on the optical absorption, shape, and size of the absorber [67]. As an absorber quickly expands on laser excitation, a strong positive initial pressure is always generated. Consequently, the early part of  $a_i(t)$  is always positive. In ultrasound imaging, as a typical scattering-based imaging modality,  $a_i(t)$  is related to the acoustic properties (density and compressibility), shape, and size of the scatterer [68]. In reality, the shape of  $a_i(t)$  is relatively random. The amplitude of an A-scan can be written as

$$A(t) = \sum_{i=1}^n a_i(t) *_t h(\bar{r}_i, t - |\bar{r}_i|/c), \quad (4.1)$$

where  $*_t$  denotes convolution in the time domain, and  $c$  denotes the propagation velocity of the ultrasonic wave. When Eq. (4.1) is applied to ultrasound imaging, round trip delays and multiple scattering are neglected because they are not key factors in our discussions. The instantaneous power of an A-scan is  $P(t) = A^2(t)$ , and the ensemble average of  $P(t)$  becomes (see Appendix D)

$$\langle P(t) \rangle = \rho_0 \int_V \left\langle \left\langle \left( a_i(t) *_t h(\bar{r}, t - |\bar{r}|/c) \right)^2 \right\rangle_i \right\rangle d\bar{r}^3 + \rho_0^2 \langle b_i(t) b_j(t) \rangle_{i \neq j}, \quad (4.2)$$

where  $b_i(t) = \langle a_i(t) \rangle *_t \int_V h(\bar{r}, t - |\bar{r}|/c) d\bar{r}^3$ ,  $\rho$  is the particle density,  $V$  is the structure volume,  $\langle \rangle_i$  is averaging over all  $n$  particles, and  $\langle \rangle_{i \neq j}$  is averaging over all particle pairs.

The first term in Eq. (4.2) is the sum of the powers of the waves generated from all particles. Therefore, it is called the uncorrelated contribution to the total power. It represents the power of the random fluctuations—speckle, which is shared in both imaging modalities. Speckle in ultrasound imaging has been widely used for tissue characterization.

The second term in Eq. (4.2) is responsible for the prominent boundary features in photoacoustic images. Because this term represents the correlations among the particles, it is responsible for the correlated contribution to the total power. First, the correlated power appears only as boundary features, because  $\int_V h(\vec{r}, t - |\vec{r}|/c) d\vec{r}^3$  is always zero inside the structure (see Appendix E). Second, the correlated power exists in photoacoustic images but usually disappears in ultrasound images. As stated above,  $a_i(t)$  in PAT always starts with a positive value, which produces strong correlations among the absorbers. After averaging over all particle pairs, the correlated power shows up as strong boundary features in PAT. In ultrasound imaging, however, the polarity of  $a_i(t)$  is relatively random. After averaging, the correlated power usually becomes negligible.

Equation (4.2) can be further simplified by assuming the particles to be point targets. The photoacoustic wave from each point target excited by a delta laser pulse becomes  $a_i(t) = a_i \delta'(t)$ , where each  $a_i$  is a random variable with a positive mean [6]. In ultrasound imaging, researchers usually assume  $a_i(t) = a_i \delta(t)$ , where each  $a_i$  is a zero mean random variable because the scattered signal is due to fluctuations in acoustic properties relative to the mean [69, 70]. By substituting  $a_i(t) = a_i \delta'(t)$  or  $a_i(t) = a_i \delta(t)$  into Eq. (4.2), we have

$$\langle P(t) \rangle = (\bar{C}^2 + \sigma_C^2) \rho \int_V (\tilde{h}(\vec{r}, t - |\vec{r}|/c))^2 d\vec{r}^3 + \bar{C}^2 \rho^2 \left( \int_V \tilde{h}(\vec{r}, t - |\vec{r}|/c) d\vec{r}^3 \right)^2. \quad (4.3)$$

Here,  $\bar{C}$  and  $\sigma_C$  are the mean and the standard deviation of the absorbing cross section of the unit optical absorber or the backscattering coefficient of the unit

scatterer, and  $\tilde{h}(\vec{r}, t)$  is the spatiotemporal system impulse response. Since integral with  $\delta'(t)$  denotes differentiation with respect to time, we have  $\tilde{h}(\vec{r}, t) = h'(\vec{r}, t)$  in PAT and  $\tilde{h}(\vec{r}, t) = h(\vec{r}, t)$  in ultrasound imaging. The unit optical absorber is characterized by the optical absorbing cross section, which quantifies its photon energy absorbing capability, as the amplitude of the PA wave (ultrasonic wave) is proportional to the optical energy deposition. In comparison, the unit scatterer is characterized by the backscattering coefficient, which represents the changes in both amplitudes and phases of the incident wave. For Rayleigh scatterers, the phase change to the backscattered wave is either 0 or  $\pi$ ; therefore, the backscattering coefficient can be either positive or negative. The backscattering coefficient should not be confused with the scattering cross section, which indicates the scattering capability to the wave energy and is always positive.

From Eq. (4.3), we can quantify the visibility of the interior speckle in PAT, which is defined as the ratio of the square root of the average speckle power to the magnitude of boundary features, which are composed of both uncorrelated and correlated powers. The uncorrelated power is proportional to  $\rho$ , while the correlated power is proportional to  $\rho^2$ . When  $\rho$  is sufficiently large, the correlated power is much stronger than the uncorrelated power, and the speckle visibility in PAT is approximately inversely proportional to  $\sqrt{\rho}$ . In this case, the correlated power dominates the photoacoustic image.

We should note that Eq. (4.3) explains the differences in contrast mechanisms for PAT and US. In PAT, the average absorption cross section is always greater than zero ( $\bar{C} > 0$ ), and the correlated power dominates the uncorrelated power for large  $\rho$ . As a consequence, the PA signal amplitude is approximately proportional to the optical absorption coefficient  $\mu_a = \bar{C}\rho$  of the absorbing target. Similarly, when imaging a soft-tissue–bone interface with US from the soft-tissue side, the average backscattering coefficient is always positive ( $\bar{C} > 0$ ) and the correlated power dominates. When

imaging soft tissue structures with US, however, researchers usually assume that the average backscattering coefficient is zero ( $\bar{C} = 0$ ) [70], which is because the scattered signals are due to fluctuations in acoustic properties relative to the mean. Substituting  $\bar{C} = 0$  into Eq. (1) nullifies the second term on the right-hand side:

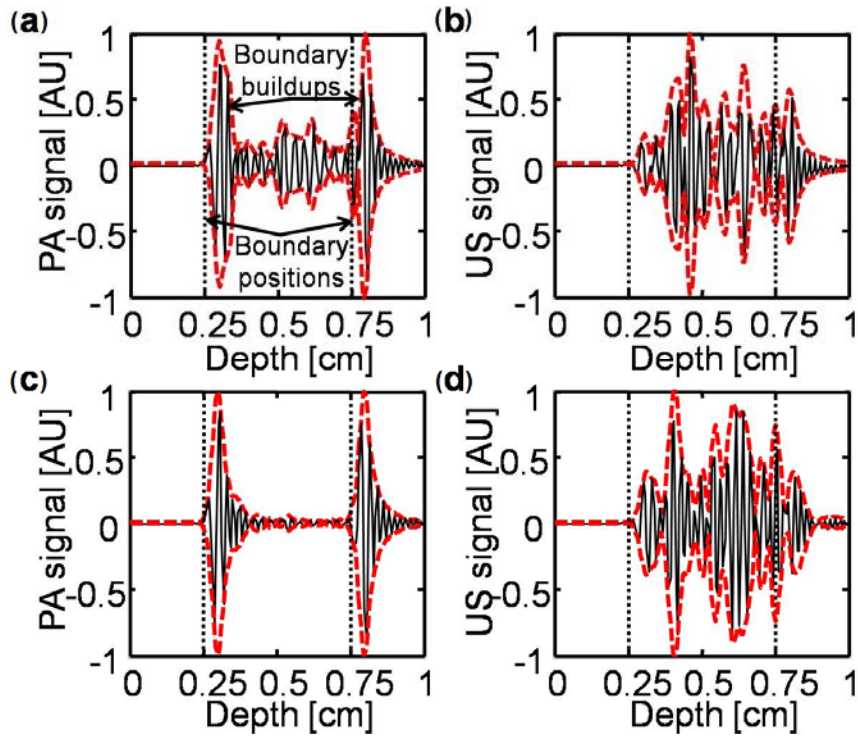
$$\langle P(t) \rangle = \sigma_c^2 \rho \int_V \left( \tilde{h}(\bar{r}, t - |\bar{r}|/c) \right)^2 d\bar{r}^3. \quad (4.4)$$

As a result, US clearly relies on speckle contrast when imaging soft tissues.

#### 4.1.4 Simulation Studies

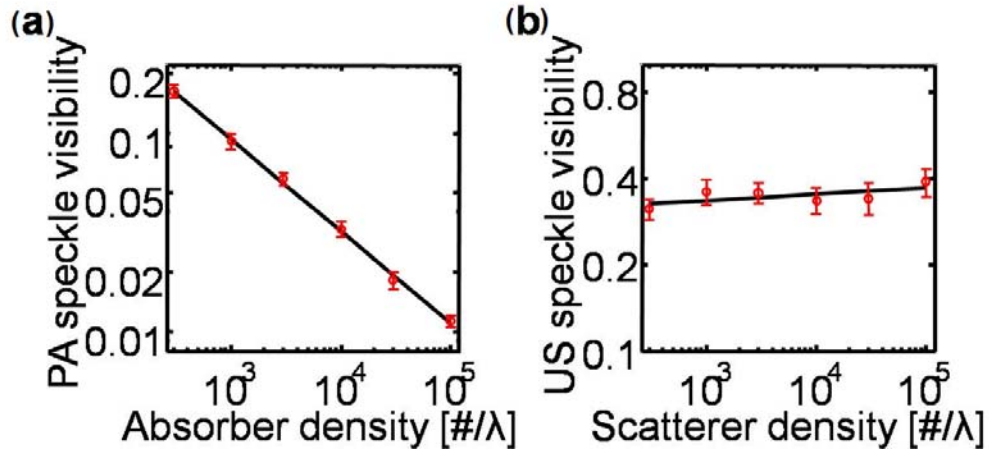
We use simulation to further illustrate our analysis. Our numerical phantom contains a 5 mm thick tissue structure, whose center is located 5 mm away from the transducer surface. It is composed of a large number of absorbers randomly distributed between 2.5 mm and 7.5 mm along the ultrasonic axis. The transducer is assumed to have 5 MHz central frequency with 100% bandwidth.

Figure 4.2 compares the photoacoustic profile with the ultrasound profile, where the exact boundary positions are marked as vertical dotted lines. The envelopes represent the magnitude of absorption or scattering. Between Figs. 4.2(a) and 4.2(b), the object has the same particle density. In the photoacoustic A-scan [Fig. 4.2(a)], we notice two prominent semi-deterministic boundaries, which dominate the random speckle fluctuations in between. The separation between either maximum profile position and the corresponding boundary position is a fraction of the center ultrasonic wavelength. In the ultrasonic A-scan [Fig. 4.2(b)], the speckle fluctuations spread across the entire imaged object, and no outstanding boundaries are observed.



**Figure 4.2** Simulated depth profiles of a slab. **(a)** PAT, absorber density:  $1,000/\lambda$ ; **(b)** Ultrasound imaging, scatterer density:  $1,000/\lambda$ ; **(c)**, PAT, absorber density:  $100,000/\lambda$ ; **(d)**, Ultrasound imaging, scatterer density:  $100,000/\lambda$ .  $\lambda$ : the acoustic wavelength of 5 MHz ultrasound. PA: Photoacoustic; US: Ultrasound.

In PAT, the visibility of the interior speckle was also found to decrease with increase in absorber density, as demonstrated in Figs. 4.2(a) and 4.2(c) and further quantified in Fig. 4.3(a). The linear fit between the logarithm of the speckle visibility and the absorber density has a slope of  $-0.479 \pm 0.003$ , which is close to the inverse square-root dependence as predicted above. By contrast, the speckle visibility stays approximately constant in the ultrasound images, as illustrated in Figs. 4.2(b) and 4.2(d) and further quantified in Fig. 4.3(b). In both Figs. 4.2(a) and 4.2(c), each middle segment—between the two outermost minima of the profile within the two maxima—proves to be a fully developed speckle, because the magnitude of the photoacoustic signal follows the Rayleigh distribution and the intensity follows the exponential distribution. Therefore, the simulation confirms the aforementioned explanations.



**Figure 4.3 Relationship between the speckle visibility in photoacoustic/ultrasound imaging and the absorber/scatterer density. (a) PAT; (b) Ultrasound imaging.** Error bars: standard errors of the means (circles) based on 10 realizations of particle distributions; solid lines: linear fits. PA: Photoacoustic; US: Ultrasound.

In Figs. 4.4(a) and 4.4(b) we present simulated photoacoustic and ultrasonic cross-sectional images (B-scan) of a round tumor, where the exact boundaries of the tumors are plotted as dashed lines. The ultrasound spatial-temporal response of the 5 MHz focused ultrasonic transducer is calculated by the Field II program. We first simulate the case when the absorbing or scattering strength of the particles in the tumor area is 10 times that of the background particles. For a large tumor with a diameter of 2 mm, strong signals at its top and bottom boundaries are observed in the photoacoustic B-scan [Fig. 4.4(a)]. The side boundaries are missing due to the limited view of the linear detection geometry. Figure 4.4(b) shows the corresponding ultrasonic B-scan image, where speckle artifacts prevail. The higher scattering strength of the tumor induces a stronger speckle in the tumor area, which suppresses the background speckle. In reality, a 10:1 scattering strength contrast is usually unavailable in ultrasound imaging. Therefore, the background speckle may be more prominent.



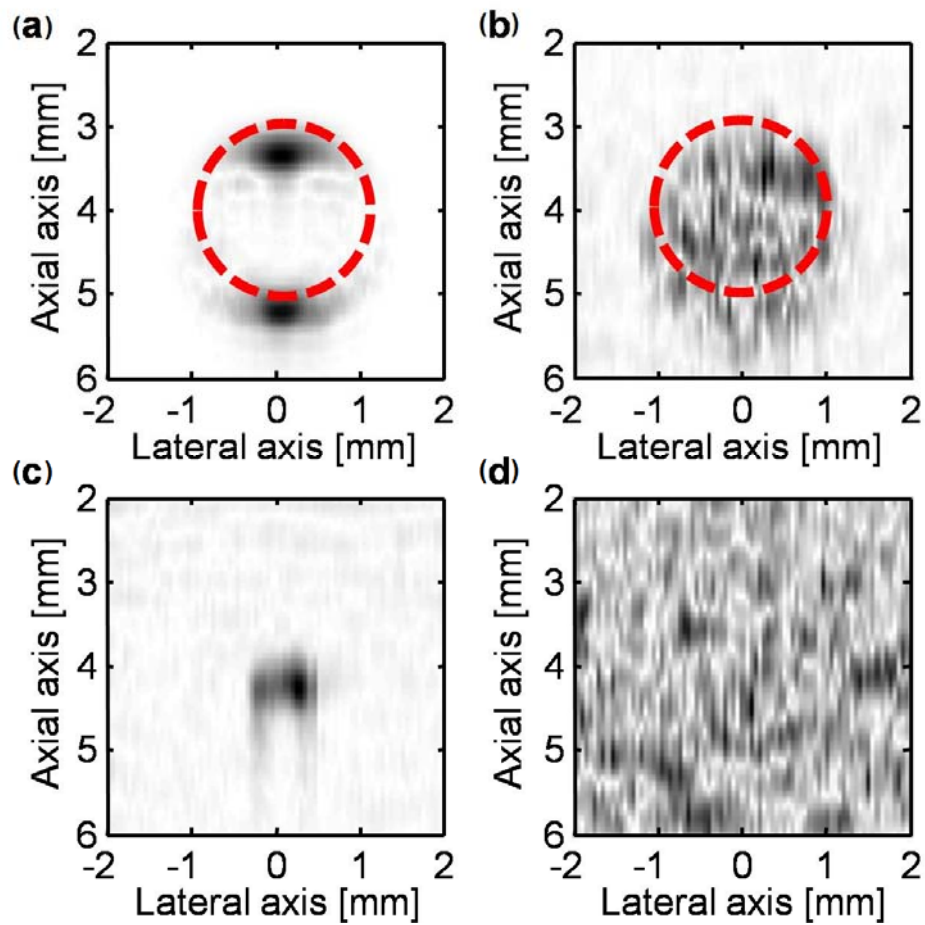


**Figure 4.4 Simulated cross-sectional photoacoustic and ultrasonic images of round tumors.** Photoacoustic/ultrasonic B-scans of tumors with 2 mm diameter [(a)/(b)] and 100  $\mu\text{m}$  diameter [(c)/(d)]. Absorber/scatterer density: 5 million/ $\mu\text{L}$ . Absorbing/scattering strength contrast: 10:1.

In Figs. 4.4(c) and 4.4(d), respectively, the photoacoustic and ultrasonic B-scans of a sub-resolution-sized tumor with a diameter of 100  $\mu\text{m}$  are shown. In Fig. 4.4(c), the small tumor appears in the photoacoustic B-scan image as a solid area without distinct front and back boundaries. In Fig. 4.4(d), the tumor cannot be identified in the ultrasonic B-scan image. As expected, the interior speckle is further suppressed in the photoacoustic image, whereas the visibility of speckle remains unchanged in the ultrasound image.

## 4.2 PAT Speckle Dependence on Boundary Roughness

As we discussed in the previous section 4.1, for scattering-based coherent imaging, two conditions must be met to ensure specular reflection. First, all scatterers on the surface must have similar properties so that the polarity changes to the incident wave due to backscattering are the same. Second, the boundary roughness must be less than  $\lambda/4$ —with  $\lambda$  being the center wavelength—so that the phase-delay variations due to scatterer spatial distribution differences are within  $\pi$ .

PAT naturally satisfies the first condition for “specular emission”. However, the second condition might be violated in rare cases. A natural question is whether the boundary signals in PAT can become fully developed speckles if the absorbing target has sufficiently rough boundaries, which is addressed in section 4.2.

To analyze the effect of boundary roughness on PAT speckles, we simulate PAT of absorbing objects with boundaries having various degrees of roughness, which is quantified by the root-mean-squared (RMS) value ( $\delta$ ) and the correlation length ( $\xi$ ) of the boundary height [71]. Our numerical phantoms are composed of a large number of absorbers, which are statistically independently and homogeneously distributed inside and outside the absorbing objects. The absorbers inside the absorbing objects have 5 times the average cross sections of those in the background. The boundary-profile functions of the absorbing objects are assumed to follow a stationary Gaussian stochastic process. The mean and the standard deviation of the stochastic process represent the mean boundary location and the standard deviation of the surface height (the RMS value  $\delta$ ), respectively. The correlation function of the stochastic process is  $G(\bar{r} - \bar{r}') = \exp\left(-|\bar{r} - \bar{r}'|^2 / \xi^2\right)$ , where  $\bar{r}$  and  $\bar{r}'$  represent two position vectors on the mean boundary plane. Numerically, a boundary profile function is generated by

convolving a zero-mean Gaussian distribution of random numbers for the surface height with the Gaussian correlation function [71].

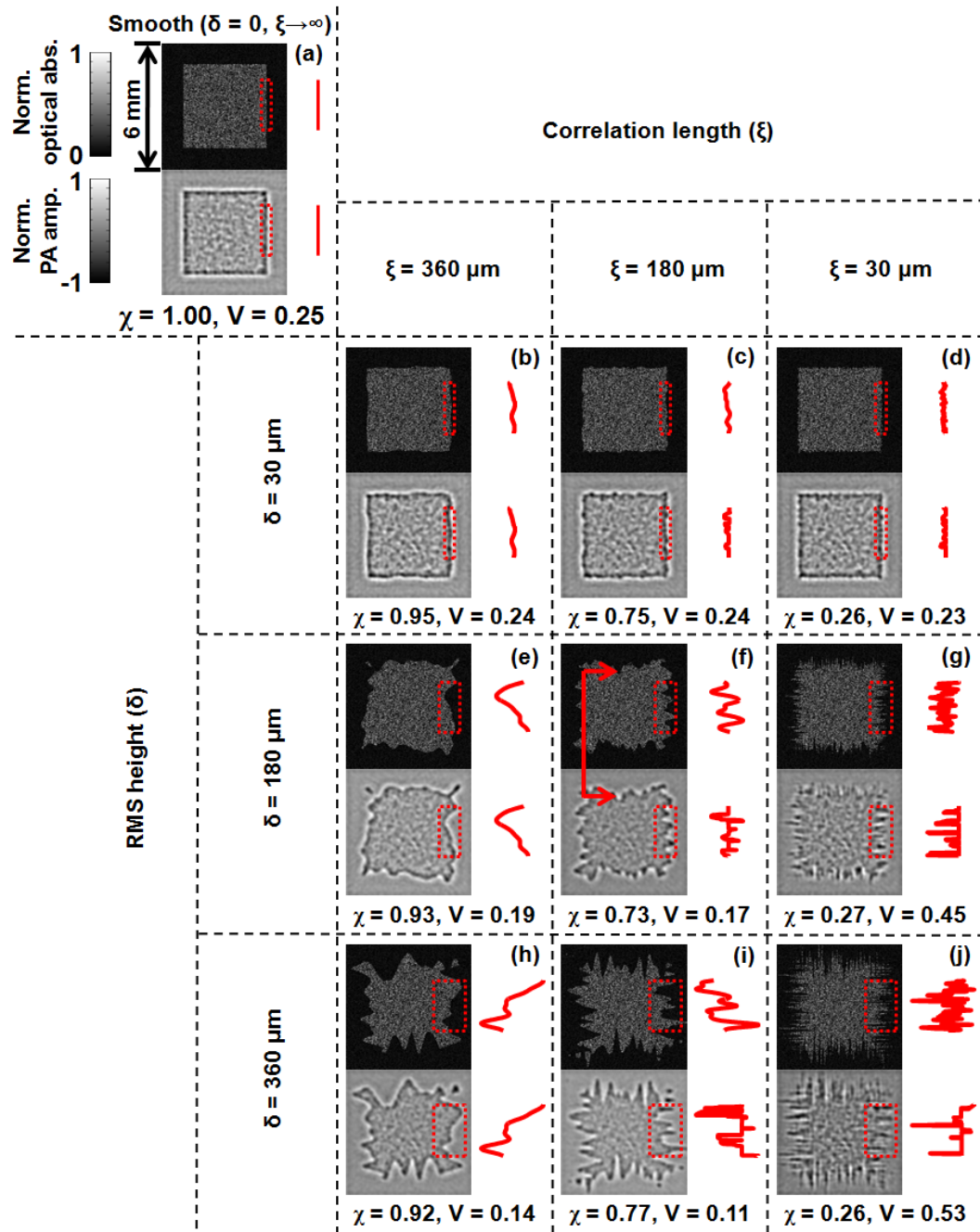


**Figure 4.5 Simulated PAT of absorbing targets with boundaries having various degrees of roughness at a spatial resolution of 180  $\mu\text{m}$ .** The boundary roughness is quantified by the RMS value ( $\delta$ ) and the correlation length ( $\xi$ ) of the boundary height. **(a)** PAT of absorbing targets with smooth boundaries. **(b)–(j)** PAT of absorbing targets with rough boundaries. In each cell, the simulated absorber distribution is plotted in the top row, and the corresponding PAT image is shown in the bottom row. Segments of the boundaries from both plots are plotted as surface height versus lateral position (solid curves). The correlation coefficient ( $\gamma$ ) between the true and the reconstructed boundaries as well as the speckle visibility ( $V$ ) is computed.

The PAT simulation parameters are set to the same values as those of a custom-designed 512-element ring-array PAT system [72]. Each ultrasonic transducer element is cylindrically focused in the elevational direction; therefore, an in-plane two-dimensional (2D) image can be reconstructed. The simulated mechanical-electrical impulse response (EIR) has a center frequency of 5 MHz (100% bandwidth). Using the Field II program [69, 70], we calculate the spatiotemporal response of every ultrasonic transducer element due to all the absorbers in the imaging region. The PAT image is then reconstructed from these spatiotemporal responses [30]. The in-plane spatial resolution, i.e., the full-width-at-half-maximum (FWHM) of the point spread function (PSF), is  $\sim 180 \mu\text{m}$ .

The simulation results are tabulated by the RMS height  $\delta$  and the correlation length  $\xi$  in Fig. 4.5. As the RMS height  $\delta$  increases, the boundary height fluctuates more; as the correlation length  $\xi$  decreases, the position of each point on the boundary becomes less correlated with that of its neighbors; if  $\delta = 0$  or  $\xi \rightarrow \infty$ , the boundary becomes perfectly smooth [Fig. 4.5(a)]. Each cell of the table shows the true absorber distribution at the top and the corresponding reconstructed PAT image at the bottom. Segments of the boundaries of the absorbing objects within the dashed frames are extracted and shown as solid curves with a horizontal magnification of two times. The reconstructed PAT images show observable boundary buildups as well as interior speckles. In Fig. 4.5(a) ( $\xi \rightarrow \infty$ ), and Figs. 4.5(b), 4.5(e), and 4.5(h) ( $\xi = 360 \mu\text{m}$ , which equals twice the

in-plane resolution), the reconstructed and true boundaries agree well (correlation coefficient  $\chi = 0.92 - 0.95$ ) while the visibility of interior speckles ( $V$ ) decreases slightly with increasing  $\delta$ . In Figs. 4.5(c), 4.5(f), and 4.5(i) ( $\xi = 180 \mu\text{m}$ , which equals the in-plane resolution), some of the features of the true boundaries cannot be recovered by the reconstructed boundaries ( $\chi = 0.73 - 0.77$ ). In Figs. 4.5(d), 4.5(g), and 4.5(j) ( $\xi = 30 \mu\text{m}$ , which equals  $1/6$  of the in-plane resolution), the height fluctuations of the reconstructed and true boundaries become less correlated ( $\chi = 0.26 - 0.27$ ). Moreover, the amplitude of the reconstructed boundary vanishes with increasing  $\delta$ , increasing the visibility of interior speckles. In all the cases, however, the average powers of the interior speckles without normalization to the boundary signals are equal. Therefore, the variations in speckle visibilities are due to the changes in the amplitudes of the reconstructed boundaries

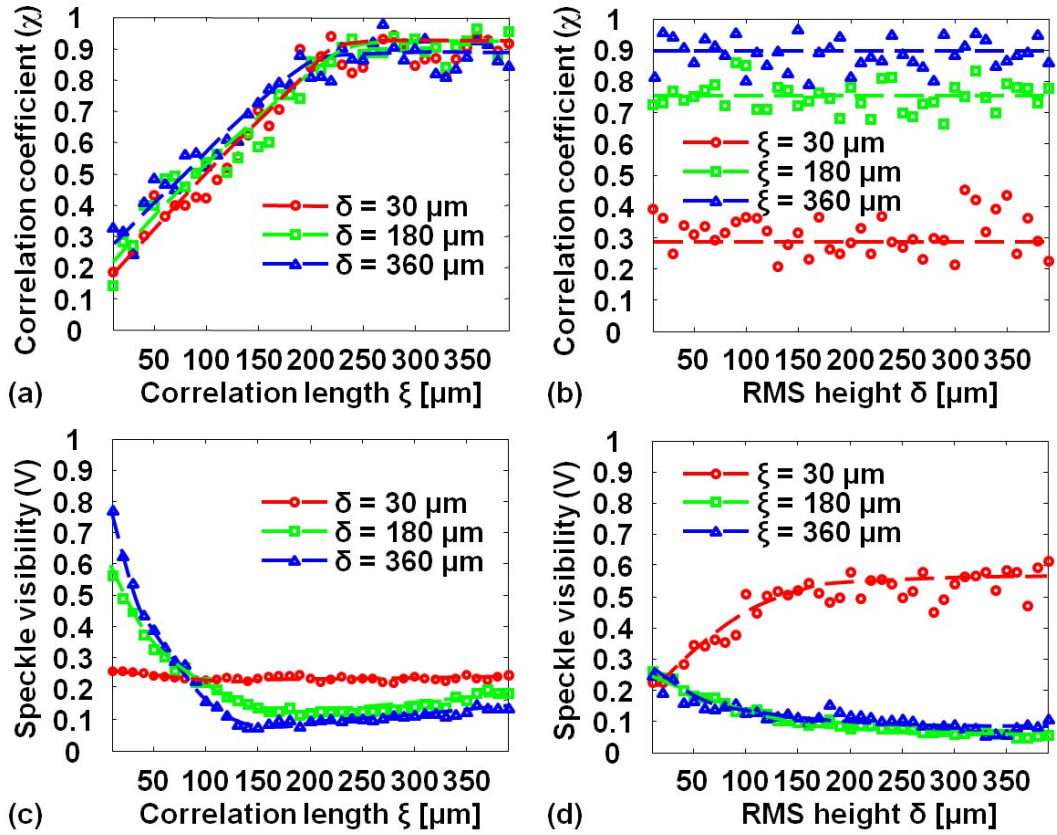


**Figure 4.6 Effects of the RMS height ( $\delta$ ) and the correlation length ( $\xi$ ) on PA image boundaries.** Effects of **(a)** the correlation length ( $\xi$ ) and **(b)** the RMS height ( $\delta$ ) on the correlation coefficient ( $\chi$ ) between the real and the reconstructed boundaries. Effects of **(c)** the correlation ( $\xi$ ) length and **(d)** the RMS height ( $\delta$ ) on the speckle visibility ( $V$ ).

In Figs. 4.6(a) and 4.6(b), the correlation coefficient ( $\chi$ ) between the reconstructed and the true boundary profiles is quantified as functions of the correlation length  $\xi$  and the RMS height  $\delta$ . We found that  $\chi$  depends solely on  $\xi$  because the correlation coefficient between  $\chi$  and  $\delta$  is 0.08. If  $\xi > 180 \mu\text{m}$  (the in-plane resolution), all the boundary features can be resolved, and thus the reconstructed boundaries agree with the true boundaries. Conversely, if  $\xi < 180 \mu\text{m}$  (the in-plane resolution), features are too fine to be resolved. Therefore, even when the boundary fluctuations are small ( $\delta = 30 \mu\text{m}$ ), the reconstructed boundaries do not agree with the true boundaries.

In Figs. 4.6(c) and 4.6(d), the speckle visibility ( $V$ ) is plotted as functions of the correlation length  $\xi$  and the RMS height  $\delta$ . Because the interior speckle amplitudes follow Gaussian distribution, we define boundary features as the reconstructed image regions that have magnitudes more than three time of the standard deviation of the interior speckle amplitudes. We found that  $V$  depends on both  $\xi$  and  $\delta$ . In Fig. 4.6(c),  $V$  decreases as  $\xi$  increases when  $\xi < 180 \mu\text{m}$  (the in-plane resolution). If the correlation lengths are smaller than the in-plane resolution, shorter correlation lengths usually introduce more randomized phase-delay variations, especially when the RMS heights are larger than the in-plane resolution so that effective roughness presents. An extreme example is that if  $\xi \ll 180 \mu\text{m}$  and  $\delta \gg 180 \mu\text{m}$  the reconstructed boundaries become fully developed speckles and the speckle visibility  $V \rightarrow 1$ . As  $\xi$  increases further, the speckle visibilities  $V$  at various  $\delta$  gradually converge to the value of  $V$  for the smooth boundary, because  $\xi \rightarrow \infty$  indicates smooth boundaries regardless of  $\delta$ . In Fig. 4.6(d), if  $\xi < 180 \mu\text{m}$ ,  $V$  increases as  $\delta$  increases, which

introduces more randomized phase-delay variations. If  $\xi \geq 180 \mu\text{m}$ , however, some reconstructed boundary segments [e.g., the paired arrows in Fig. 4.5(f)] have higher signal strengths than the reconstructed smooth flat boundaries. The geometric shapes of these features match the ring-shaped ultrasonic detection aperture, and therefore the phase variations of the PA partial waves from the surface absorbers are smaller than those from the smooth flat boundaries. As a result, the average boundary strengths of these boundaries are slightly higher than those of smooth boundaries, and thus the speckle visibilities are slightly lower.

The analysis above indicates that PAT speckles may appear in rare cases. For example, we may observe speckles when imaging melanoma, if the melanoma has rough boundaries whose correlation length is much smaller than and the RMS value is much greater than the imaging resolution. In contrast, when imaging blood vessels with most of the PAT systems (center frequencies ranging from 1 MHz to 75 MHz), we observe only the boundary signals. The blood vessel walls or red blood cells are considered smooth on the scale of the acoustic wavelengths, and the interior speckles are suppressed by the prominent boundary signals.

### 4.3 Experimental Validations

We used the same ring-array based PAT system [72, 73] to experimentally study the statistics of PAT speckles. The illumination source was a tunable pulsed laser system based on an optical parametric oscillator (OPO; Vibrant HE 315I, Opotek, Inc.). The laser pulse had a repetition rate of 10 Hz and a pulse width of 5 ns. After collimation, the laser beam was homogenized through a ground glass before it reached the top surface of the tissue phantom. The absorbing objects were made of gelatin (10% gelatin by weight) mixed with graphite particles in various concentrations.

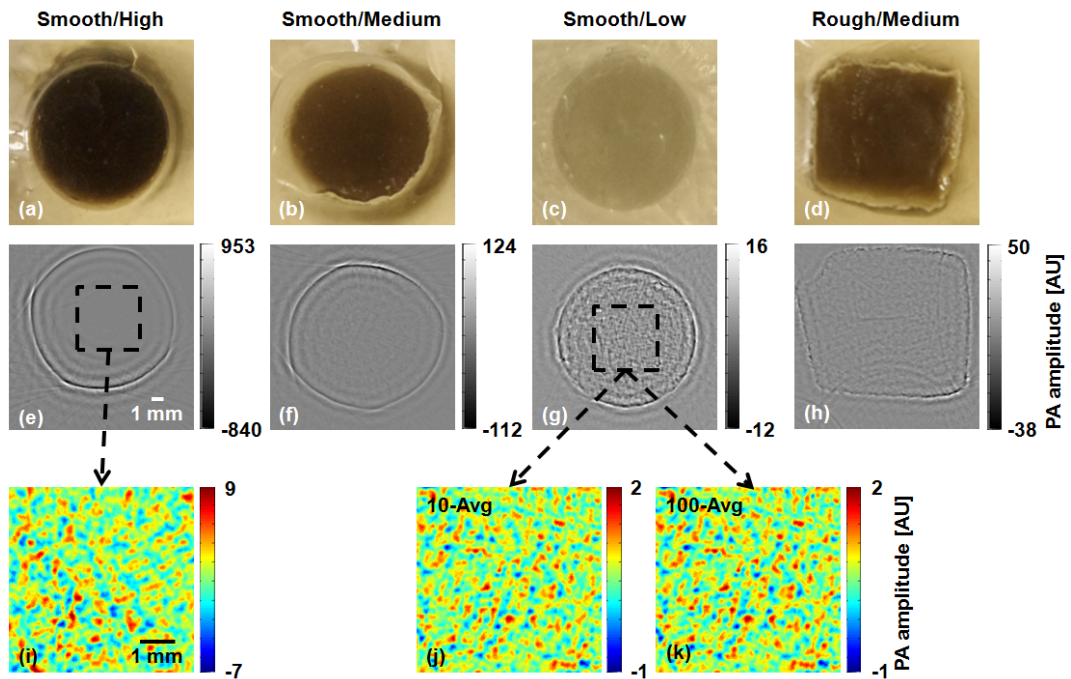


**Figure 4.7 Phantom experiments.** Photographs of gelatin phantoms with smooth boundaries and with (a) high, (b) medium, and (c) low graphite particle concentrations. (d) Photograph of a gelatin phantom with rough boundaries and with medium graphite particle concentration. (e)–(h) Corresponding PAT images obtained with a ring-array PAT system. (i)–(k) Interior PAT speckle patterns.

Photographs of the phantoms with high, medium, and low graphite particle concentrations and with smooth boundaries are shown in Figs. 4.7(a)–4.7(c). The corresponding PAT images are shown in Figs. 4.7(e)–4.7(g). As predicted in our previous study, we observed strong boundary buildups, which suppress the internal speckle patterns [Fig. 4.7(i)]. Also, the boundary features are most prominent at the highest particle concentration [Fig. 4.7(e)], and interior speckles become noticeable at the medium particle concentration [Fig. 4.7(f)] and become apparent at the lowest particle concentration [Fig. 4.7(g)]. The phantom with low particle concentration was imaged 10 times and 100 times, and the averaged reconstructed interior textures are shown in Figs. 4.7(j) and 4.7(k). Because both the phantom and the imaging system are



stationary in each experiment, such averaging does not diminish the speckles but does reduce random noises. The similarity between the two interior images, with a correlation coefficient of 0.996, confirms that the interior texture is due to speckles rather than random noises. For comparison, a phantom with medium particle concentration and rough boundaries [Fig. 4.7(d)] was studied, where both the correlation length  $\xi$  and the RMS height  $\delta$  of the boundary profile are  $\sim 60 \mu\text{m}$ . In the PAT images of the phantoms, the rough boundaries [Fig. 4.7(h)] produced 2.8 times weaker boundary amplitudes than the smooth boundaries at the same particle concentration [Fig. 4.7(f)].

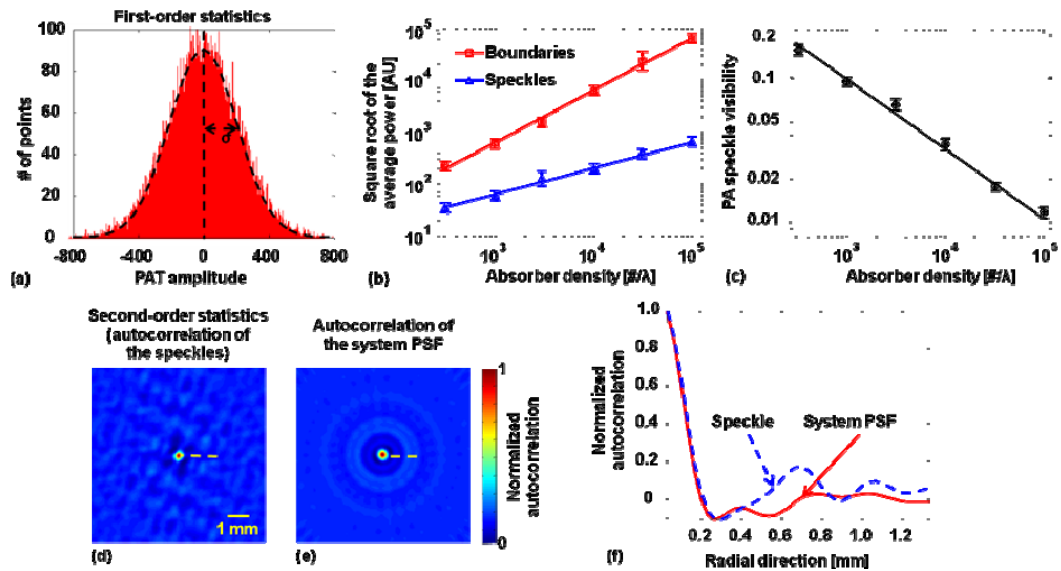


**Figure 4.8 Experimental PAT speckle statistics.** (a) First-order speckle statistics. (b) Dependence of the square root of the average powers of both the boundaries (red solid line) and the interiors (blue solid line) in the PAT images on the absorber density. (c) Dependence of the PA speckle visibility on the absorber density. (d) Second-order speckle statistics. (e) Auto-correlation of the system PSF. (f) One-dimensional radial plots of the auto-correlation of the speckles and the auto-correlation of the system PSF.

We quantified the first order statistic of the PA speckles by plotting the histogram of the interior speckle amplitude (without the envelope detection) [Fig. 4.8(a)]. Since the coherent interference of ultrasonic waves can be described as a random walk process,

the amplitude of the PA speckles follows a Gaussian distribution. The mean of the speckle amplitude is zero, because the PSF does not contain DC. The standard deviation of the Gaussian distribution ( $\sigma$ ) which represents the square root of the average speckle power, is proportional to the product of the average particle absorption cross section  $\bar{C}$  and the square root of the particle concentration ( $\sqrt{\rho}$ ). In Fig. 4.8(b), we show that  $\sigma$  is proportional to  $\sqrt{\rho}$ , while the boundary magnitude is proportional to  $\rho$ . As a consequence, the speckle visibility ( $V$ ) is inversely proportional to the square root of the particle density  $\sqrt{\rho}$  [51] for smooth boundary targets [Fig. 4.8(c)].

The second-order statistic of the speckles is shown in Fig. 4.8(d). In the classic speckle theory, the autocorrelation of the fully developed speckle pattern carries only the information of the system PSF rather than that of the target texture. The autocorrelation of the system PSF is shown in Fig. 4.8(e), which agrees with the autocorrelation of the speckle patterns [Fig. 4.8(f)].

## 4.4 Discussions and Conclusions

We should clarify the definition of absorbers. In our model, unit absorbers must be 1) much smaller than the resolution cell and 2) statistically independently and homogeneously distributed in locations within a resolution cell. For example, when imaging blood vessels with a 5 MHz PAT system ( $\sim 180 \mu\text{m}$  in resolution), we treat red blood cells (RBCs,  $\sim 8 \mu\text{m}$  in diameter and  $\sim 2 \mu\text{m}$  in thickness) as unit absorbers. Hemoglobin molecules, however, should not be treated as unit absorbers because their aggregation in RBCs differentiates their spatial distributions inside and outside RBCs and violates condition 2. When imaging water with megahertz PAT systems, individual water molecules can be defined as unit absorbers. We can also group every  $K$  water molecules to form sparser super unit absorbers with a number density of  $\rho_{sup} = \rho / K$  as long as the dimension of the super unit absorber is much less than the resolution.

The absorption cross section of the super unit absorber  $C_{Sup}$  is the sum of the absorption cross sections ( $C$ ) of the  $K$  unit absorbers:

$$C_{Sup} = KC. \quad (4.5)$$

The location of the super unit absorber is the centroid of the locations of the unit absorbers. The super unit absorbers give rise to approximately the same image. Substituting Eq. (4.5) into Eq. (4.3), we have  $\left(\overline{C_{Sup}^2} + \sigma_{C_{Sup}}^2\right)\rho_{Sup} = \left(\overline{C}^2 + \sigma_C^2\right)\rho$  for the speckle term and  $\overline{C_{Sup}^2}\rho_{Sup}^2 = \overline{C}^2\rho^2 = \mu_a^2$  for the boundary term. Therefore, the grouping leads to statistically equivalent results without violating our theory.

In conclusion, PAT suppresses speckles by building up prominent boundary signals, via a mechanism similar to that of specular reflection. When imaging smooth boundary absorbing targets, the speckle visibility in PAT, which is defined as the ratio of the square root of the average power of speckles to that of boundaries, is inversely proportional to the square root of the absorber density. If the surfaces of the absorbing targets have uncorrelated height fluctuations, however, the boundary features may become fully developed speckles. The findings were validated by simulations and experiments. The first- and second-order statistics of PAT speckles were also studied experimentally. While the amplitude of the speckles follows a Gaussian distribution, the autocorrelation of the speckle patterns tracks that of the system point spread function.

# Chapter 5

## Conclusions

### 5.1 Summary of the Work Done

The work presented in this dissertation can be divided into three parts. The first part focused on quantitative PAT. The second part focused on applying the compressed sensing theory to PAT reconstruction. The third part focused on the PAT speckle theory.

**Quantitative PAT:** We demonstrated the feasibility of using the acoustic spectrum information to quantify optical absorption *in vivo* with OR-PAM in the optical ballistic regime and with AR-PAM in the optical diffusive regime. To the best of our knowledge, this is the first time acoustic spectrum information was used for PA quantitative study. This method is self-calibrating and thus is insensitive to absolute optical fluence. By taking advantage of the cancellation effect, the acoustic attenuation and system limited bandwidth can be corrected with multi-wavelength measurements. Moreover, this method can quantify the absolute value of  $\mu_a$ , which can be used to quantify hemoglobin concentrations in absolute units.

**Compressed sensing in PAT:** By incorporating the compressed sensing theory in the PAT reconstruction, we can effectively reduce the number of DAQ channels. Both the phantom and the *in vivo* results show that the compressed sensing method can

effectively reduce the undersampling artifacts. By incorporating the compressed sensing theory in the PAT reconstruction, we can effectively reduce the system cost, or cover a larger FOV with the same number of measurements.

**PAT speckles:** We found that speckle artifacts in PAT are suppressed by prominent boundary buildups. The theory has been explained from three aspects and validated by both simulation and experiments. The initial all-positive photoacoustic pressure rises provide strong correlation among the absorbers, which gives rise to strong boundary buildups. While images from ultrasound imaging and all other scattering-based imaging modalities are dominated by uncorrelated power, photoacoustic images are dominated by correlated power. We have also discussed the effect of boundary roughness on PAT speckles. The correlation coefficient ( $\chi$ ) and the speckle visibility ( $V$ ) were quantified as functions of the boundary correlation length ( $\xi$ ) and the boundary RMS height ( $\delta$ ). Our analysis hold for all PAT implementations considering the linearity of the PA imaging process, the conclusions

## 5.2 Directions for Future Work

**For Quantitative PAT:** Quantification of optical absorption coefficients from the acoustic spectra can be applied to other reflection-mode PAT system setups, such as PAT array systems [74], for  $sO_2$  and [HBT] quantifications.

**For Compressed sensing in PAT:** To further improve the reconstruction, the ultrasonic transducer mechanical-electrical impulse response (EIR) as well as the spatial impulse response (SIR) should be included in the model [75].

**For PAT speckles:** The speckle contrast can be used to quantify the absorber density. Moreover, the standard deviation of speckles is proportional to the absorption cross section of absorbers and thus can be used to quantify the absorption cross section of

the nano particles. The proposed method is sensitive only to optical absorption [76] and does not require calibrations. PAT speckles can also be used in tissue characterization. The speckles may also be useful for skull aberration correction [77].

## Appendix A

# Relative Sensitivity of DOT to Optical Absorption Coefficient

We estimate the relative sensitivity of DOT ( $S_{DOT\_a}$ ) to optical absorption coefficient ( $\mu_a$ ) based on the frequency domain DOT systems. The formulas used here can be found in Chapter 11 of *Biomedical Optics: Principles and Imaging* written by L. V. Wang and H. Wu (Wiley, Hoboken, NJ, 2007).

We use  $\mu_a(\vec{r}_j)$  and  $\mu_s'(\vec{r}_j)$  to denote the  $\mu_a$  and  $\mu_s'$  at location  $\vec{r}_j$ , and the diffusion coefficient  $D(\vec{r}_j) = 1/[3(\mu_a(\vec{r}_j) + \mu_s'(\vec{r}_j))]$ . The background  $\mu_a$  and  $\mu_s'$  are expressed as  $\mu_{a0}$  and  $\mu_{s0}'$ , and the background diffusion coefficient  $D_0 = 1/[3(\mu_{a0} + \mu_{s0}')]$ . We use  $\delta\mu_a(\vec{r}_j)$ ,  $\delta\mu_s'(\vec{r}_j)$ , and  $\delta D(\vec{r}_j)$  to denote the heterogeneities relative to  $\mu_{a0}$ ,  $\mu_{s0}'$ , and  $D_0$ , respectively [i.e.,  $\mu_a(\vec{r}_j) = \mu_{a0} + \delta\mu_a(\vec{r}_j)$ ,  $\mu_s'(\vec{r}_j) = \mu_{s0}' + \delta\mu_s'(\vec{r}_j)$ ,  $D(\vec{r}_j) = D_0 + \delta D(\vec{r}_j)$ ]. To simplify the problem, we assume that the Born approximation is valid, which means the heterogeneities are weak relative to the background.

DOT measures a quantity directly related to the AC photon density  $U_{AC}(\vec{r}_d, \vec{r}_s)$ , where  $\vec{r}_d$  and  $\vec{r}_s$  are the locations of the detector and the source, respectively. For the

detector-source pair located at  $(\bar{r}_d, \bar{r}_s)$ , the differential AC photon density wave

$\delta U_{AC}(\bar{r}_d, \bar{r}_s)$  due to the heterogeneity  $\delta\mu_a(\bar{r}_j)$  can be expressed as

$$\delta U_{AC}(\bar{r}_d, \bar{r}_s) = W_{a,j} \delta\mu_a(\bar{r}_j), \quad (\text{A.1})$$

where

$$\delta U_{AC}(\bar{r}_d, \bar{r}_s) = U_{AC}(\bar{r}_d, \bar{r}_s) - U_0(\bar{r}_d, \bar{r}_s), \quad (\text{A.2})$$

$$\delta\mu_a(\bar{r}_j) = \mu_a(\bar{r}_j) - \mu_{a0}, \quad (\text{A.3})$$

$$\text{and } W_{a,j} = -\frac{G_0(\bar{r}_d, \bar{r}_j) U_0(\bar{r}_j, \bar{r}_s) \Delta x \Delta y \Delta z}{D_0}. \quad (\text{A.4})$$

Here,  $G_0(\bar{r}_d, \bar{r}_j)$  denotes the Green function associated with the diffusion equation and  $U_0(\bar{r}_d, \bar{r}_s)$  denotes the AC photon density, and both are for a homogeneous medium that has the background optical properties.  $\Delta x$ ,  $\Delta y$ , and  $\Delta z$  represent the sizes of the grid elements along the  $x$ ,  $y$ ,  $z$  directions, respectively.

A small perturbation on the object  $\mu_a(\bar{r}_j)$  causes a change to the measurement quantity  $U_{AC}(\bar{r}_d, \bar{r}_s)$ .  $S_{DOR\_a}$  is defined as the fractional change of  $U_{AC}(\bar{r}_d, \bar{r}_s)$  divided by the fractional change of  $\mu_a(\bar{r}_j)$  as

$$S_{DOR\_a} = \left| \frac{\Delta U_{AC}(\bar{r}_d, \bar{r}_s)}{U_{AC}(\bar{r}_d, \bar{r}_s)} / \frac{\Delta \mu_a(\bar{r}_j)}{\mu_a(\bar{r}_j)} \right|. \quad (\text{A.5})$$

Taking the derivatives on both sides of Eqs. (A.1), (A.2), and (A.3) yields

$$\Delta \delta U_{AC}(\bar{r}_d, \bar{r}_s) = W_{a,j} \Delta \delta \mu_a(\bar{r}_j), \quad (\text{A.6})$$

$$\Delta \delta U_{AC}(\bar{r}_d, \bar{r}_s) = \Delta U_{AC}(\bar{r}_d, \bar{r}_s), \quad (\text{A.7})$$

$$\text{and } \Delta \delta \mu_a(\bar{r}_j) = \Delta \mu_a(\bar{r}_j). \quad (\text{A.8})$$

Substituting Eqs. (A.7) and (A.8) into Eq. (A.6) yields



$$\Delta U_{AC}(\bar{r}_d, \bar{r}_s) = W_{a,j} \Delta \mu_a(\bar{r}_j). \quad (\text{A.9})$$

Substituting Eq. (A.9) into Eq. (A.5) yields

$$S_{DOT\_a} = \left| \frac{\mu_a(\bar{r}_j) W_{a,j}}{U_{AC}(\bar{r}_d, \bar{r}_s)} \right|. \quad (\text{A.10})$$

Substituting Eq. (A.4) and  $U_{AC}(\bar{r}_d, \bar{r}_s) \approx U_0(\bar{r}_d, \bar{r}_s)$  (Born Approximation) into Eq. (A.10) yields

$$S_{DOT\_a} = \left| \frac{\mu_a(\bar{r}_j) G_0(\bar{r}_d, \bar{r}_j) U_0(\bar{r}_j, \bar{r}_s) \Delta x \Delta y \Delta z}{D_0 U_0(\bar{r}_d, \bar{r}_s)} \right|. \quad (\text{A.11})$$

To further simply the problem without loss of generality, we use the Green function for a point source in an infinite medium, and

$$G_0(\bar{r}_d, \bar{r}_j) = \frac{\exp(ik_0 |\bar{r}_d - \bar{r}_j|)}{4\pi |\bar{r}_d - \bar{r}_j|}, \quad (\text{A.12})$$

$$U_0(\bar{r}, \bar{r}_s) = \frac{B}{cD_0} \frac{\exp(ik_0 |\bar{r} - \bar{r}_s|)}{4\pi |\bar{r} - \bar{r}_s|}. \quad (\text{A.13})$$

Here  $k_0$  is the propagation constant of the photon-density wave and  $c$  is the speed of light in the medium.  $|B|$  is the AC source amplitude and  $B = |B| \exp(-i\omega t - \phi_B)$  with  $\phi_B$  being the phase. Substituting Eqs. (A.12) and (A.13) into Eq. (A.11) yields

$$S_{DOT\_a} = \frac{3}{4\pi} \frac{|\bar{r}_d - \bar{r}_s|}{|\bar{r}_d - \bar{r}_j| |\bar{r}_j - \bar{r}_s|} \Delta x \Delta y \Delta z (\mu_{a0} + \mu_{s0}') \mu_a(\bar{r}_j). \quad (\text{A.14})$$

From Eq. (A.14), we conclude:

- 1) The relative sensitivity  $S_{DOT\_a}$  is higher if  $\frac{|\bar{r}_d - \bar{r}_s|}{|\bar{r}_d - \bar{r}_j| |\bar{r}_j - \bar{r}_s|}$  is larger. If the distances from the voxel of interest to both the source ( $|\bar{r}_j - \bar{r}_s|$ ) and the detector ( $|\bar{r}_d - \bar{r}_j|$ ) are shorter, the relative sensitivity is higher. However, for non-invasive DOT, the

source and detector can be placed only outside the tissue, and thus these distances are limited by the target depth. In transmission mode, it can be shown that

$$\frac{|\bar{r}_d - \bar{r}_s|}{|\bar{r}_d - \bar{r}_j| |\bar{r}_j - \bar{r}_s|} = \frac{1}{|\bar{r}_j - \bar{r}_s|} \left( \frac{|\bar{r}_d - \bar{r}_s| - |\bar{r}_d - \bar{r}_j|}{|\bar{r}_d - \bar{r}_j|} + 1 \right) \leq \frac{1}{|\bar{r}_d - \bar{r}_j|} + \frac{1}{|\bar{r}_j - \bar{r}_s|}.$$

The equality holds and the maximum sensitivity occurs if and only if  $\bar{r}_s$ ,  $\bar{r}_d$ , and  $\bar{r}_j$  are in line, and  $\bar{r}_j$  is between  $\bar{r}_s$  and  $\bar{r}_d$ .

- 2) The relative sensitivity  $S_{DOT\_a}$  is higher if  $\Delta x \Delta y \Delta z$  is larger. For sufficiently large uniformly absorbing objects, defining larger imaging voxels yield higher  $S_{DOT\_a}$ . However, when the imaging voxel is defined to be even larger than the absorbing object, the absorption coefficient of the object is volume-averaged with the background absorption coefficient.
- 3) The relative sensitivity  $S_{DOT\_a}$  is higher if  $\mu_{a0} + \mu_{s0}'$  is larger; i.e., the background absorption coefficient and reduced scattering coefficient are larger.
- 4) The relative sensitivity  $S_{DOT\_a}$  is higher if  $\mu_a(\bar{r}_j)$  is larger; i.e. the object absorption coefficient is larger.

For practical values of these parameters,  $|\bar{r}_d - \bar{r}_s| = 3 \text{ cm}^{-1}$ ,  $|\bar{r}_d - \bar{r}_j| = 1.5 \text{ cm}^{-1}$ ,  $|\bar{r}_j - \bar{r}_s| = 1.5 \text{ cm}^{-1}$ ,  $\Delta x \Delta y \Delta z = 5 \times 5 \times 5 \text{ mm}^3$  (voxel size),  $\mu_{s0}' = 10 \text{ cm}^{-1}$ ,  $\mu_{a0} = 0.1 \text{ cm}^{-1}$  (background optical properties), and  $\mu_a(\bar{r}_j) = 0.11 \text{ cm}^{-1}$  (voxel optical absorption coefficient heterogeneity is 10% relative to that of the background) the relative sensitivity of DOT to  $\mu_a$  is  $S_{DOT\_a} \approx 0.044$ .

In photoacoustic tomography (PAT), the measurement is directly proportional to the optical absorption coefficient. As a consequence, the relative sensitivity to the optical absorption coefficient is always 1 in PAT [11]. Therefore, DOT is usually much less sensitive to the optical absorption coefficient than PAT.

## Appendix B

# Validation of Equation (2.8) with Monte Carlo Simulations

The analytical solution of the fluence decay in blood [Eq. (2.8)] was validated by Monte Carlo simulations. The simulated object was assumed to be composed of two layers, while the top layer is the background tissue and the bottom layer is the blood. The optical properties of the background tissue are set to be  $\mu_a = 0.1 \text{ cm}^{-1}$ ,  $\mu_s = 100 \text{ cm}^{-1}$  and  $g = 0.9$ , while those of the blood are set to be  $\mu_a = 200 \text{ cm}^{-1}$ ,  $\mu_s = 30 \text{ cm}^{-1}$ , and  $g = 0.995$  [52]. Here  $\mu_a$  is the absorption coefficient,  $\mu_s$  is the scattering coefficient, and  $g$  is the anisotropy factor. The thickness of the background tissue is 0.2 cm, which is greater than the transport mean free path ( $l_t' = 0.1 \text{ cm}$ ). Therefore, the photons are almost completely diffused when they reach the blood layer.

In Fig. B. 1, the fluence decay profile in blood is plotted on a log scale, and it matches the analytical solution given by Eq. (2.8).

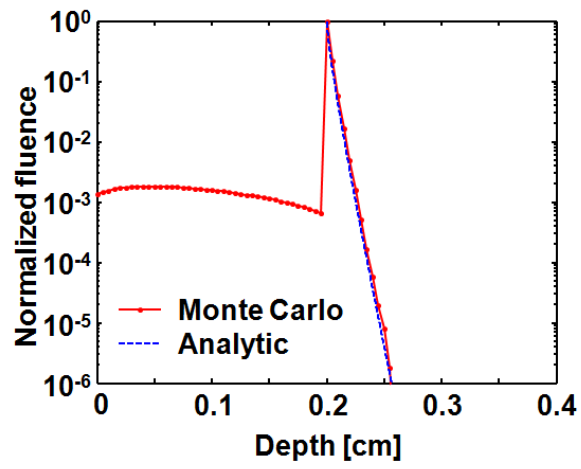


Fig. B.1. Comparison of the Monte Carlo simulation result and the analytical solution.

# Appendix C

## Compressed Sensing Reconstruction

### Algorithm

In this section, we describe the reconstruction algorithm for solving the constrained optimization problem, which has been proved to be closely related to solving the following convex unconstrained optimization problem [78]:

$$\min_x f(x) = \frac{1}{2} \|\Phi x - y\|_2^2 + \lambda \|\Psi x\|_1, \quad (\text{C.1})$$

where  $\lambda$  is a nonnegative regularization parameter, which determines the trade-off between the data consistency and the sparsity. In order for these two problems to be equivalent,  $\varepsilon$  and  $\lambda$  must satisfy a special relationship. However, it is difficult to find analytical solutions if the matrix  $A = \Phi\Psi^*$  is not orthogonal [78]. Therefore, we solved a series of  $\lambda$  to find a suboptimal solution. The process is described as follows:

**Step 1:** Let  $\lambda = 0.05 \|A^T y\|_\infty$  [61], and solve the problem (C.1) for  $x$ .

**Step 2:** Check the condition  $\|\Phi x - y\|_2 < \varepsilon$ . If this condition holds, we increase  $\lambda$  to promote the sparsity  $\|\Psi x\|_1$ ; otherwise we decrease  $\lambda$  to enforce the data consistency  $\|\Phi x - y\|_2$ .

**Step 3:** Problem (C.1) is solved again with the new  $\lambda$ . Previously solved  $x$  is used as the initial guess. By using this warm starting technique [61], the current optimization process takes much fewer numbers of iterations than the previous one.

**Step 4:** Steps 2) and 3) are repeated for multiple times.

The final solution is still only a suboptimal solution. However, problem (C.1) can be solved with the conjugate gradient descent method with backtracking line search method [58], which is computationally efficient to implement.

The forward problem matrix  $\Phi$  is extremely large that direct matrix operation is computationally impractical. Therefore, the computations of both  $\Phi$  and its transpose  $\Phi^T$  were implemented as sub-modules.

## Appendix D

### Derivation of the Speckle Visibility Equation

$$A(t) = \sum_{i=1}^n a_i(t - |\bar{r}_i|/c) *_t h(\bar{r}_i, t) = \sum_{i=1}^n a_i(t) *_t h(\bar{r}_i, t - |\bar{r}_i|/c)$$

The instantaneous power of an A-scan is

$$P(t) = A^2(t) = \sum_{i=1}^n \sum_{j=1}^n \left[ a_i(t) *_t h(\bar{r}_i, t - |\bar{r}_i|/c) \right] \left[ a_j(t) *_t h(\bar{r}_j, t - |\bar{r}_j|/c) \right].$$

$P(t)$  can be separated into two groups of terms:

$$P(t) = \sum_{i=1}^n \left[ a_i(t) *_t h(\bar{r}_i, t - |\bar{r}_i|/c) \right]^2 + \sum_{i=1}^n \sum_{j=1, j \neq i}^n \left[ a_i(t) *_t h(\bar{r}_i, t - |\bar{r}_i|/c) \right] \left[ a_j(t) *_t h(\bar{r}_j, t - |\bar{r}_j|/c) \right].$$

The ensemble average of  $P(t)$  is

$$\langle P(t) \rangle = \left\langle \sum_{i=1}^n \left[ a_i(t) *_t h(\bar{r}_i, t - |\bar{r}_i|/c) \right]^2 \right\rangle + \left\langle \sum_{i=1}^n \sum_{j=1, j \neq i}^n \left[ a_i(t) *_t h(\bar{r}_i, t - |\bar{r}_i|/c) \right] \left[ a_j(t) *_t h(\bar{r}_j, t - |\bar{r}_j|/c) \right] \right\rangle.$$

The first group on the left hand side (uncorrelated contribution/speckle term) can be simplified as

$$\left\langle \sum_{i=1}^n \left[ a_i(t) *_t h(\bar{r}_i, t - |\bar{r}_i|/c) \right]^2 \right\rangle$$

$$\begin{aligned}
&= \sum_{i=1}^n \left\langle \left[ a_i(t) *_t h(\bar{r}_i, t - |\bar{r}_i|/c) \right]^2 \right\rangle \\
&= \sum_{i=1}^n \int_V \frac{\rho}{n} \left\langle \left| a_i(t) *_t h(\bar{r}, t - |\bar{r}|/c) \right|^2 \right\rangle d\bar{r}^3
\end{aligned}$$

(The probability density function of  $\bar{r}_i$  is  $f_{\bar{r}_i}(\bar{r}) = \begin{cases} \frac{\rho}{n} & \bar{r} \in V \\ 0 & \bar{r} \notin V \end{cases}$ )

$$\begin{aligned}
&= \rho \int_V \frac{\sum_{i=1}^n \left\langle \left| a_i(t) *_t h(\bar{r}, t - |\bar{r}|/c) \right|^2 \right\rangle}{n} d\bar{r}^3 \\
&= \rho \int_V \left\langle \left\langle \left| a_i(t) *_t h(\bar{r}, t - |\bar{r}|/c) \right|^2 \right\rangle \right\rangle_i d\bar{r}^3
\end{aligned}$$

The second group, responsible for correlated contribution, on the left hand side can be simplified as

$$\begin{aligned}
&\left\langle \sum_{i=1}^n \sum_{j=1, j \neq i}^n \left[ a_i(t) *_t h(\bar{r}_i, t - |\bar{r}_i|/c) \right] \left[ a_j(t) *_t h(\bar{r}_j, t - |\bar{r}_j|/c) \right] \right\rangle \\
&= \sum_{i=1}^n \sum_{j=1, j \neq i}^n \left\langle \left[ a_i(t) *_t h(\bar{r}_i, t - |\bar{r}_i|/c) \right] \left[ a_j(t) *_t h(\bar{r}_j, t - |\bar{r}_j|/c) \right] \right\rangle_{j \neq i} \\
&= \sum_{i=1}^n \sum_{j=1, j \neq i}^n \int_V \int_V \frac{\rho^2}{n(n-1)} \left[ \langle a_i(t) \rangle *_t h(\bar{r}_1, t - |\bar{r}_1|/c) \right] \left[ \langle a_j(t) \rangle *_t h(\bar{r}_2, t - |\bar{r}_2|/c) \right] d\bar{r}_1^3 d\bar{r}_2^3
\end{aligned}$$

(The probability density function of  $\bar{r}_i, \bar{r}_j: f_{\bar{r}_i, \bar{r}_j, i \neq j}(\bar{r}_1, \bar{r}_2) = \begin{cases} \frac{\rho^2}{n(n-1)} & \bar{r}_1 \neq \bar{r}_2 \in V \\ 0 & \bar{r}_1, \bar{r}_2 \notin V \end{cases}$ )

$$\begin{aligned}
&= \sum_{i=1}^n \sum_{j=1, j \neq i}^n \frac{\rho^2}{n(n-1)} \left[ \langle a_i(t) \rangle *_t \int_V h(\bar{r}_1, t - |\bar{r}_1|/c) d\bar{r}_1^3 \right] \left[ \langle a_j(t) \rangle *_t \int_V h(\bar{r}_2, t - |\bar{r}_2|/c) d\bar{r}_2^3 \right] \\
&= \rho^2 \frac{\sum_{i=1}^n \sum_{j=1, j \neq i}^n \left[ \langle a_i(t) \rangle *_t \int_V h(\bar{r}, t - |\bar{r}|/c) d\bar{r}^3 \right] \left[ \langle a_j(t) \rangle *_t \int_V h(\bar{r}, t - |\bar{r}|/c) d\bar{r}^3 \right]}{n(n-1)} \\
&= \rho^2 \left\langle \left[ \langle a_i(t) \rangle *_t \int_V h(\bar{r}, t - |\bar{r}|/c) d\bar{r}^3 \right] \left[ \langle a_j(t) \rangle *_t \int_V h(\bar{r}, t - |\bar{r}|/c) d\bar{r}^3 \right] \right\rangle_{i \neq j}
\end{aligned}$$

Therefore, the ensemble average of  $P(t)$  can be derived as:



$$\begin{aligned}
\langle P(t) \rangle &= \rho \int_V \left\langle \left\langle \left| a_i(t) *_{t} h(\bar{r}, t - |\bar{r}|/c) \right|^2 \right\rangle \right\rangle_i d\bar{r}^3 \\
&+ \rho^2 \left\langle \left[ \langle a_i(t) \rangle *_{t} \int_V h(\bar{r}, t - |\bar{r}|/c) d\bar{r}^3 \right] \left[ \langle a_j(t) \rangle *_{t} \int_V h(\bar{r}, t - |\bar{r}|/c) d\bar{r}^3 \right] \right\rangle_{i \neq j}
\end{aligned}$$

## Appendix E

### Explanation of $\int_V h(\vec{r}, t - |\vec{r}|/c) d\vec{r}^3 = 0$ inside the structure

The spatial-temporal response  $h(\vec{r}, t)$  is separable in the focal zone, and we can assume  $h(\vec{r}, t) = h_1(\vec{r})h_2(t)$ . For a focused ultrasonic transducer, the extent of the spatial response  $h_1(\vec{r})$  can be approximated by a cylinder aligned with the focal zone. Within the cylinder,  $h_1(\vec{r})$  is approximately constant. Therefore, we have

$$g(t) = \int_V h(\vec{r}, t - |\vec{r}|/c) d\vec{r}^3 = \int_V h_1(\vec{r})h_2(t - |\vec{r}|/c) d\vec{r}^3 \propto \int_{V_C} h_2(t - |\vec{r}|/c) d\vec{r}^3,$$

where  $V_C$  is the volume of the cylinder. We use  $Z_1$  and  $Z_2$  to denote the axial positions of the front and back boundaries of  $V$ . Therefore, we have

$$g(t) \propto \int_{V_C} h_2(t - |\vec{r}|/c) d\vec{r}^3 \propto \int_{Z_1}^{Z_2} h_2(t - |\vec{r}|/c) d|\vec{r}| = \int_{t-Z_2/c}^{t-Z_1/c} h_2(s) ds.$$

The transducer does not have a DC component, therefore  $\int_0^{t_h} h_2(t) dt = 0$ , where  $[0, t_h]$  is the duration of the temporal impulse response. When the signals from inside the structure ( $Z_1/c < t = t_0 < Z_2/c$ ) are received, we usually have  $t_0 - Z_1/c \gg t_h$ . Therefore,

$$g(t_0) \propto \int_{t_0-Z_2/c}^{t_0-Z_1/c} h_2(s) ds = \int_0^{t_0-Z_1/c} h_2(s) ds \approx 0.$$

However, if the signal is received from the boundaries,  $t_0 - Z_1 / c < t_n$ . The partial integration of  $h_2(s)$  results in a non-zero value

## References

- [1] B. Venkatesh, R. Meacher, M. J. Muller, T. J. Morgan, and J. Fraser, "Monitoring tissue oxygenation during resuscitation of major burns," *Journal of Trauma-Injury Infection and Critical Care*, vol. 50, pp. 485-493, (2001).
- [2] A. A. Tandara and T. A. Mustoe, "Oxygen in wound healing - More than a nutrient," *World Journal of Surgery*, vol. 28, pp. 294-300, (2004).
- [3] C. Menon and D. L. Fraker, "Tumor oxygenation status as a prognostic marker," *Cancer Letters*, vol. 221, pp. 225-235, (2005).
- [4] H. F. Zhang, K. Maslov, M. Sivaramakrishnan, G. Stoica, and L. V. Wang, "Imaging of hemoglobin oxygen saturation variations in single vessels in vivo using photoacoustic microscopy," *Applied Physics Letters*, vol. 90, p. 053901, (2007).
- [5] M. Sivaramakrishnan, K. Maslov, H. F. Zhang, G. Stoica, and L. V. Wang, "Limitations of quantitative photoacoustic measurements of blood oxygenation in small vessels," *Physics in Medicine and Biology*, vol. 52, pp. 1349-1361, (2007).
- [6] L. V. Wang and H. Wu, *Biomedical Optics: Principles and Imaging*. Hoboken, NJ: Wiley, (2007).
- [7] B. Chance, E. Borer, A. Evans, G. Holtom, J. Kent, M. Maris, K. McCully, J. Northrop, and M. Shinkwin, "Optical and Nuclear-Magnetic-Resonance Studies of Hypoxia in Human Tissue and Tumors," *Annals of the New York Academy of Sciences*, vol. 551, pp. 1-16, (1988).

- [8] K. Maslov, H. F. Zhang, S. Hu, and L. V. Wang, "Optical-resolution photoacoustic microscopy for in vivo imaging of single capillaries," *Opt Lett*, vol. 33, pp. 929-31, (2008).
- [9] L. V. Wang, "Multiscale photoacoustic microscopy and computed tomography," *Nat Photonics*, vol. 3, pp. 503-509, (2009).
- [10] H. F. Zhang, K. Maslov, G. Stoica, and L. V. Wang, "Functional photoacoustic microscopy for high-resolution and noninvasive in vivo imaging," *Nature Biotechnology*, vol. 24, pp. 848-851, (2006).
- [11] L. V. Wang, "Tutorial on photoacoustic microscopy and computed tomography," *Ieee Journal of Selected Topics in Quantum Electronics*, vol. 14, pp. 171-179, (2008).
- [12] K. Maslov, H. F. Zhang, and L. V. Wang, "Effects of wavelength-dependent fluence attenuation on the noninvasive photoacoustic imaging of hemoglobin oxygen saturation in subcutaneous vasculature in vivo," *Inverse Problems*, vol. 23, pp. S113-S122, (2007).
- [13] B. T. Cox, J. G. Laufer, and P. C. Beard, "The challenges for quantitative photoacoustic imaging," presented at the Proc. SPIE, (2009).
- [14] J. Laufer, D. Delpy, C. Elwell, and P. Beard, "Quantitative spatially resolved measurement of tissue chromophore concentrations using photoacoustic spectroscopy: application to the measurement of blood oxygenation and haemoglobin concentration," *Physics in Medicine and Biology*, vol. 52, pp. 141-168, (2007).

- [15] Z. Yuan and H. B. Jiang, "Quantitative photoacoustic tomography: Recovery of optical absorption coefficient maps of heterogeneous media," *Applied Physics Letters*, vol. 88, p. 231101, (2006).
- [16] A. Q. Bauer, R. E. Nothdurft, T. N. Erpelding, L. V. Wang, and J. P. Culver, "Quantitative photoacoustic imaging: correcting for heterogeneous light fluence distributions using diffuse optical tomography," *J Biomed Opt*, vol. 16, p. 096016, (2011).
- [17] P. D. Kumavor, C. Xu, A. Aguirre, J. Gamelin, Y. Ardeshirpour, B. Tavakoli, S. Zanganeh, U. Alqasemi, Y. Yang, and Q. Zhu, "Target detection and quantification using a hybrid hand-held diffuse optical tomography and photoacoustic tomography system," *J Biomed Opt*, vol. 16, p. 046010, (2011).
- [18] R. O. Esenaliev, I. V. Larina, K. V. Larin, D. J. Deyo, M. Motamedi, and D. S. Prough, "Optoacoustic technique for noninvasive monitoring of blood oxygenation: a feasibility study," *Applied Optics*, vol. 41, pp. 4722-4731, (2002).
- [19] J. Laufer, C. Elwell, D. Delpy, and P. Beard, "In vitro measurements of absolute blood oxygen saturation using pulsed near-infrared photoacoustic spectroscopy: accuracy and resolution," *Physics in Medicine and Biology*, vol. 50, pp. 4409-4428, (2005).
- [20] Y. Y. Petrov, I. Y. Petrova, I. A. Patrikeev, R. O. Esenaliev, and D. S. Prough, "Multiwavelength optoacoustic system for noninvasive monitoring of cerebral venous oxygenation: a pilot clinical test in the internal jugular vein," *Optics Letters*, vol. 31, pp. 1827-1829, (2006).
- [21] Y. Wang and R. K. Wang, "Photoacoustic recovery of an absolute optical absorption coefficient with an exact solution of a wave equation," *Physics in Medicine and Biology*, vol. 53, pp. 6167-6177, (2008).

- [22] R. A. Kruger, D. R. Reinecke, and G. A. Kruger, "Thermoacoustic computed tomography—technical considerations," *Medical Physics*, vol. 26, pp. 1832-1837, (1999).
- [23] L. H. V. Wang, X. Zhao, H. Sun, and G. Ku, "Microwave-induced acoustic imaging of biological tissues," *Review of Scientific Instruments*, vol. 70, pp. 3744-3748, (1999).
- [24] X. D. Wang, Y. J. Pang, G. Ku, X. Y. Xie, G. Stoica, and L. V. Wang, "Noninvasive laser-induced photoacoustic tomography for structural and functional in vivo imaging of the brain," *Nature Biotechnology*, vol. 21, pp. 803-806, (2003).
- [25] R. A. Kruger, H. E. Reynolds, W. Kiser, D. R. Reinecke, and G. A. Kruger, "Thermoacoustic computed tomography for breast imaging," *Radiology*, vol. 210, pp. 587-587, (1999).
- [26] A. A. Oraevsky, E. V. Savateeva, S. V. Solomatin, A. A. Karabutov, V. G. Andreev, Z. Gatalica, T. Khamapirad, and P. M. Henrichs, "Optoacoustic imaging of blood for visualization and diagnostics of breast cancer," presented at the Proc. SPIE, (2002).
- [27] M. H. Xu and L. V. Wang, "Photoacoustic imaging in biomedicine," *Review of Scientific Instruments*, vol. 77, p. 041101, (2006).
- [28] Y. Xu, D. Feng, and L. V. Wang, "Exact frequency-domain reconstruction for thermoacoustic tomography--I: Planar geometry," *IEEE Trans Med Imaging*, vol. 21, pp. 823-8, (2002).

- [29] Y. Xu, M. Xu, and L. V. Wang, "Exact frequency-domain reconstruction for thermoacoustic tomography--II: Cylindrical geometry," *IEEE Trans Med Imaging*, vol. 21, pp. 829-33, (2002).
- [30] M. Xu and L. V. Wang, "Universal back-projection algorithm for photoacoustic computed tomography," *Phys Rev E Stat Nonlin Soft Matter Phys*, vol. 71, p. 016706, (2005).
- [31] M. H. Xu, Y. Xu, and L. V. Wang, "Time-domain reconstruction-algorithms and numerical simulations for thermoacoustic tomography in various geometries," *Ieee Transactions on Biomedical Engineering*, vol. 50, pp. 1086-1099, (2003).
- [32] K. P. Kostli, M. Frenz, H. Bebie, and H. P. Weber, "Temporal backward projection of optoacoustic pressure transients using Fourier transform methods," *Physics in Medicine and Biology*, vol. 46, pp. 1863-1872, (2001).
- [33] R. A. Kruger, P. Y. Liu, Y. R. Fang, and C. R. Appledorn, "Photoacoustic Ultrasound (Paus) - Reconstruction Tomography," *Medical Physics*, vol. 22, pp. 1605-1609, (1995).
- [34] C. G. A. Hoelen, F. F. M. de Mul, R. Pongers, and A. Dekker, "Three-dimensional photoacoustic imaging of blood vessels in tissue," *Optics Letters*, vol. 23, pp. 648-650, (1998).
- [35] D. Finch, S. K. Patch, and Rakesh, "Determining a function from its mean values over a family of spheres," *SIAM J. Math. Anal.*, vol. 35, pp. 1213-1240, (2004).
- [36] B. T. Cox, S. R. Arridge, and P. C. Beard, "Photoacoustic tomography with a limited-aperture planar sensor and a reverberant cavity," *Inverse Problems*, vol. 23, pp. S95-S112, (2007).



- [37] J. Gamelin, A. Maurudis, A. Aguirre, F. Huang, P. Guo, L. V. Wang, and Q. Zhu, "A real-time photoacoustic tomography system for small animals " *Opt. Express*, vol. 17, pp. 10489-10498, (2009).
- [38] P. Ephrat, M. Roumeliotis, F. S. Prato, and J. J. L. Carson, "Four-dimensional photoacoustic imaging of moving targets," *Optics Express*, vol. 16, pp. 21570-21581, (2008).
- [39] P. Ephrat, L. Keenliside, A. Seabrook, F. S. Prato, and J. J. L. Carson, "Three-dimensional photoacoustic imaging by sparsearray detection and iterative image reconstruction," *Journal of Biomedical Optics*, vol. 13, pp. -, (2008).
- [40] Z. Guo, C. Li, L. Song, and L. V. Wang, "Compressed sensing in photoacoustic tomography in vivo," *J Biomed Opt*, vol. 15, p. 021311, (2010).
- [41] "Laser speckle and related phenomena. Edited by j. C. Dainty," *Appl Opt*, vol. 23, p. 2661, (1984).
- [42] J. W. Goodman, *Speckle phenomena in optics: theory and applications*. Englewood: Roberts & Company, (2007).
- [43] C. B. Burckhardt, "Speckle in Ultrasound B-Mode Scans," *Ieee Transactions on Sonics and Ultrasonics*, vol. 25, pp. 1-6, (1978).
- [44] R. F. Wagner, S. W. Smith, J. M. Sandrik, and H. Lopez, "Statistics of Speckle in Ultrasound B-Scans," *Ieee Transactions on Sonics and Ultrasonics*, vol. 30, pp. 156-163, (1983).
- [45] J. S. Lee, "Speckle Suppression and Analysis for Synthetic Aperture Radar Images," *Optical Engineering*, vol. 25, pp. 636-643, (1986).

- [46] B. Karamata, K. Hassler, M. Laubscher, and T. Lasser, "Speckle statistics in optical coherence tomography," *Journal of the Optical Society of America a-Optics Image Science and Vision*, vol. 22, pp. 593-596, (2005).
- [47] Z. Guo, S. Hu, and L. V. Wang, "Calibration-free absolute quantification of optical absorption coefficients using acoustic spectra in 3D photoacoustic microscopy of biological tissue," *Opt Lett*, vol. 35, pp. 2067-9, (2010).
- [48] H. F. Zhang, K. Maslov, and L. V. Wang, "In vivo imaging of subcutaneous structures using functional photoacoustic microscopy," *Nature Protocols*, vol. 2, pp. 797-804, (2007).
- [49] X. D. Wang, X. Y. Xie, G. N. Ku, and L. V. Wang, "Noninvasive imaging of hemoglobin concentration and oxygenation in the rat brain using high-resolution photoacoustic tomography," *Journal of Biomedical Optics*, vol. 11, p. 024015, (2006).
- [50] K. Maslov, H. F. Zhang, S. Hu, and L. V. Wang, "Optical-resolution photoacoustic microscopy for in vivo imaging of single capillaries," *Optics Letters*, vol. 33, pp. 929-931, (2008).
- [51] Z. Guo, L. Li, and L. V. Wang, "On the speckle-free nature of photoacoustic tomography," *Medical Physics*, vol. 36, (2009).
- [52] A. Roggan, M. Friebel, K. Dorschel, A. Hahn, and G. Muller, "Optical properties of circulating human blood in the wavelength range 400-2500 NM," *Journal of Biomedical Optics*, vol. 4, pp. 36-46, (1999).

- [53] L. Wang, S. L. Jacques, and L. Zheng, "MCML--Monte Carlo modeling of light transport in multi-layered tissues," *Comput Methods Programs Biomed*, vol. 47, pp. 131-46, (1995).
- [54] M. A. Anastasio, J. Zhang, D. Modgil, and P. J. La Riviere, "Application of inverse source concepts to photoacoustic tomography," *Inverse Problems*, vol. 23, pp. S21-S35, (2007).
- [55] M. H. Xu and L. V. Wang, "Universal back-projection algorithm for photoacoustic computed tomography (vol 71, art no 016706, 2005)," *Physical Review E*, vol. 75, pp. -, (2005).
- [56] M. Haltmeier, G. Zangerl, and O. Scherzer, "A Reconstruction Algorithm for Photoacoustic Imaging based on the Nonuniform FFT," presented at the Research Network FWF S105: Photoacoustic Imaging in Medicine and Biology, (2008).
- [57] E. J. Candes, J. Romberg, and T. Tao, "Robust uncertainty principles: Exact signal reconstruction from highly incomplete frequency information," *Ieee Transactions on Information Theory*, vol. 52, pp. 489-509, (2006).
- [58] M. Lustig, D. Donoho, and J. M. Pauly, "Sparse MRI: The application of compressed sensing for rapid MR imaging," *Magnetic Resonance in Medicine*, vol. 58, pp. 1182-1195, (2007).
- [59] J. Provost and F. Lesage, "The Application of Compressed Sensing for Photo-Acoustic Tomography," *Ieee Transactions on Medical Imaging*, vol. 28, pp. 585-594, (2009).

- [60] G. Paltauf, J. A. Viator, S. A. Prahl, and S. L. Jacques, "Iterative reconstruction algorithm for optoacoustic imaging," *Journal of the Acoustical Society of America*, vol. 112, pp. 1536-1544, (2002).
- [61] M. A. T. Figueiredo, R. D. Nowak, and S. J. Wright, "Gradient Projection for Sparse Reconstruction: Application to Compressed Sensing and Other Inverse Problems," *Ieee Journal of Selected Topics in Signal Processing*, vol. 1, pp. 586-597, (2007).
- [62] C. H. Li and L. V. Wang, "High-numerical-aperture-based virtual point detectors for photoacoustic tomography," *Applied Physics Letters*, vol. 93, pp. -, (2008).
- [63] L. Song, K. Maslov, R. Bitton, K. K. Shung, and L. V. Wang, "Fast 3-D dark-field reflection-mode photoacoustic microscopy in vivo with a 30-MHz ultrasound linear array," *Journal of Biomedical Optics*, vol. 13, pp. -, (2008).
- [64] Z. Guo, L. Li, and L. V. Wang, "On the speckle-free nature of photoacoustic tomography," *Med Phys*, vol. 36, pp. 4084-8, (2009).
- [65] K. H. Song and L. V. Wang, "Deep reflection-mode photoacoustic imaging of biological tissue," *J Biomed Opt*, vol. 12, p. 060503, (2007).
- [66] S. L. Chen, S. W. Huang, T. Ling, S. Ashkenazi, and L. J. Guo, "Polymer microring resonators for high-sensitivity and wideband photoacoustic imaging," *IEEE Trans Ultrason Ferroelectr Freq Control*, vol. 56, pp. 2482-91, (2009).
- [67] G. J. Diebold, T. Sun, and M. I. Khan, "Photoacoustic monopole radiation in one, two, and three dimensions," *Phys Rev Lett*, vol. 67, pp. 3384-3387, (1991).

- [68] P. M. Morse and K. U. Ingard, *Theoretical acoustics*. Princeton, N.J.: Princeton University Press, (1986).
- [69] J. A. Jensen and N. B. Svendsen, "Calculation of Pressure Fields from Arbitrarily Shaped, Apodized, and Excited Ultrasound Transducers," *Ieee Transactions on Ultrasonics Ferroelectrics and Frequency Control*, vol. 39, pp. 262-267, (1992).
- [70] J. A. Jensen, "Field: A Program for Simulating Ultrasound Systems," presented at the 10th Nordic-Baltic Conference on Biomedical Imaging Published in Medical & Biological Engineering & Computing, (1996).
- [71] J. Q. Lu, X. H. Hu, and K. Dong, "Modeling of the rough-interface effect on a converging light beam propagating in a skin tissue phantom," *Applied Optics*, vol. 39, pp. 5890-5897, (2000).
- [72] C. H. Li, A. Aguirre, J. Gamelin, A. Maurudis, Q. Zhu, and L. V. Wang, "Real-time photoacoustic tomography of cortical hemodynamics in small animals," *Journal of Biomedical Optics*, vol. 15, p. 010509, (2010).
- [73] J. Xia, Z. Guo, K. Maslov, A. Aguirre, Q. Zhu, C. Percival, and L. V. Wang, "Three-dimensional photoacoustic tomography based on the focal-line concept," *J Biomed Opt*, vol. 16, p. 090505, (2011).
- [74] T. N. Erpelding, C. Kim, M. Pramanik, L. Jankovic, K. Maslov, Z. Guo, J. A. Margenthaler, M. D. Pashley, and L. V. Wang, "Sentinel lymph nodes in the rat: noninvasive photoacoustic and US imaging with a clinical US system," *Radiology*, vol. 256, pp. 102-10, (2010).
- [75] K. Wang, S. A. Ermilov, R. Su, H. P. Brecht, A. A. Oraevsky, and M. A. Anastasio, "An imaging model incorporating ultrasonic transducer properties

- for three-dimensional optoacoustic tomography," *IEEE Trans Med Imaging*, vol. 30, pp. 203-14, (2011).
- [76] E. C. Cho, C. Kim, F. Zhou, C. M. Cobley, K. H. Song, J. Y. Chen, Z. Y. Li, L. H. V. Wang, and Y. N. Xia, "Measuring the Optical Absorption Cross Sections of Au-Ag Nanocages and Au Nanorods by Photoacoustic Imaging," *Journal of Physical Chemistry C*, vol. 113, pp. 9023-9028, (2009).
- [77] G. Montaldo, M. Tanter, and M. Fink, "Time reversal of speckle noise," *Phys Rev Lett*, vol. 106, p. 054301, (2011).
- [78] E. van den Berg and M. P. Friedlander, "Probing the Pareto Frontier for Basis Pursuit Solutions," *Siam Journal on Scientific Computing*, vol. 31, pp. 890-912, (2008).

# Vita

## Zijian Guo

<b>Date of Birth</b>	May 18, 1984
<b>Place of Birth</b>	Beijing, P.R. China
<b>Degrees</b>	Ph.D. Biomedical Engineering, May 2012 M.S. Biomedical Engineering, December 2011 B.S. Electrical Engineering, July 2006
<b>Professional Societies</b>	SPIE
<b>Publications</b>	<p>Z. Guo, C. P. Favazza, and L. V. Wang, "Quantitative photoacoustic microscopy of optical absorption coefficients from acoustic spectra in the optical diffusive regime," submitted;</p> <p>Z. Guo, Z. Xu, and L. V. Wang, "Dependence of photoacoustic speckles on boundary roughness," submitted;</p> <p>Y. Wang, T. N. Erpelding, L. Jankovic, Z. Guo, J. L. Robert, G. David, and L. V. Wang, "<i>In vivo</i> three-dimensional photoacoustic imaging based on a clinical matrix array ultrasound probe," submitted;</p> <p>L. Li, X. Cai, A. Krumholz, Z. Guo, T. N. Erpelding, Y. Zhang, Y. Xia, and L. V. Wang, "Multi-scale molecular photoacoustic tomography of gene expression," submitted;</p> <p>J. Xia, Z. Guo, K. Maslov, A. Aguirre, Q. Zhu, C. Pervical, and L. V. Wang, "Three-dimensional photoacoustic tomography based on the focal-line concept," <i>Journal of Biomedical Optics</i>, 16(9), 090506 (2011);</p> <p>L. Nie, Z. Guo, and L. V. Wang, "Photoacoustic tomography of monkey brain using virtual ultrasonic point detectors," <i>Journal of Biomedical Optics</i>, 16(7), 076005 (2011);</p> <p>Z. Guo, S. Hu, and L. V. Wang, "Calibration-free absolute quantification of optical absorption coefficients using acoustic</p>

spectra in three-dimensional photoacoustic microscopy of biological tissue," *Optics Letters*, 35(12), 2067-2069 (2010);

T. N. Erpelding, C. Kim, M. Pramanik, L. Jankovic, K. Maslov, Z. Guo, J. Margenthaler, M. Pashley, and L. V. Wang, "Noninvasive photoacoustic and ultrasonic imaging of rat sentinel lymph nodes with a clinical ultrasound system," *Radiology*, 256, 102-110 (2010);

Z. Guo, C. Li, L. Song, and L. V. Wang, "Compressed sensing in photoacoustic tomography *in vivo*," *Journal of Biomedical Optics*, 15(2), 021311 (2010);

Z. Guo, L. Li and L. V. Wang, "On the speckle-free nature of photoacoustic tomography," *Medical Physics* 36(9), 4084-4088 (2009);

May 2012



Quant. & Recon. in PAT, Guo, PH.D. 2012